AD-A135 956 SYNTHESIS AND PROPERTIES OF ELEVATED TEMPERATURE P/M ALUMINUM ALLOYS(U) NORTHWESTERN UNIV EVANSTON IL DEPT OF MATERIALS SCIENCE AND E.. M E FINE ET AL. 29 NOV 83 1/1

UNCLASSIFIED AFOSR-TR-83-1202 AFOSR-82-0005 F/G 11/6 NL

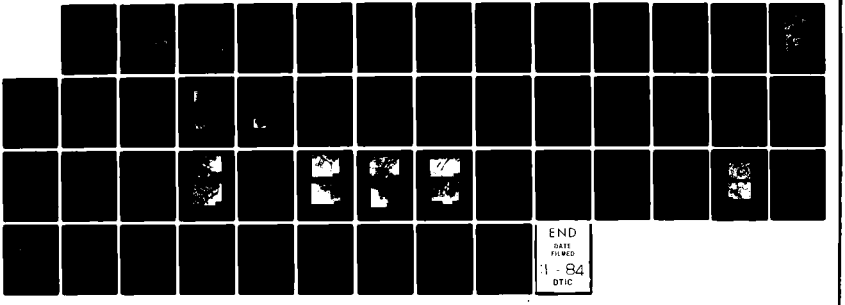

END
DATE FILMED
1 - 84
DTIC

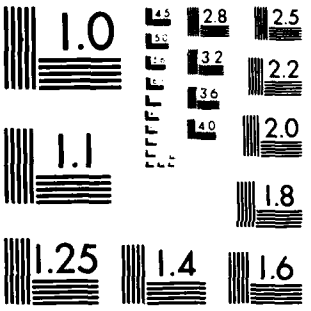

DEPARTMENT OF MATERIALS SCIENCE & ENGINEERING
THE TECHNOLOGICAL INSTITUTE
NORTHWESTERN UNIVERSITY
EVANSTON, ILLINOIS

Annual Technical Report on

Synthesis and Properties of Elevated Temperature P/M Aluminum Alloys

AF Grant No.: AFOSR-82-0005

For the Period
1 October 1982 to 30 September 1983

Principal Investigators:

Morris E. Fine, Walter P. Murphy Professor of Materials Science and Engineering (Telephone: (312) 492-5579)

Julia R. Weertman, Professor of Materials Science and Engineering (Telephone: (312) 492-5353)

November 29, 1983

UNCLASSIFIED

SECURITY CLASSIFICATION OF THIS PAGE (When Data Entered)

REPORT DOCUMENTATION PAGE	READ INSTRUCTIONS BEFORE COMPLETING FORM
1. REPORT NUMBER: AFOSR-TR- 83-1202	2. GOVT ACCESSION NO.: AD-A135956
3. RECIPIENT'S CATALOG NUMBER:	
4. TITLE (and Subtitle): SYNTHESIS AND PROPERTIES OF ELEVATED TEMPERATURE P/M ALUMINUM ALLOYS	5. TYPE OF REPORT & PERIOD COVERED: Annual Technical Report 10/1/82 - 9/30/83
	6. PERFORMING ORG. REPORT NUMBER:
7. AUTHOR(s): Morris E. Fine, Julia R. Weertman	8. CONTRACT OR GRANT NUMBER(s): AFOSR-82-0005
9. PERFORMING ORGANIZATION NAME AND ADDRESS: Northwestern University, Dept. of Materials Science & Engineering, Evanston, Illinois 60201	10. PROGRAM ELEMENT, PROJECT, TASK AREA & WORK UNIT NUMBERS: 2306/A1, 61102F
11. CONTROLLING OFFICE NAME AND ADDRESS: Air Force Office of Scientific Research /NE, Bolling AFB, Building 410, Washington, D. C. 20332	12. REPORT DATE: 11/29/83
	13. NUMBER OF PAGES:
14. MONITORING AGENCY NAME & ADDRESS (if different from Controlling Office)	15. SECURITY CLASS. (of this report): Unclassified
	15a. DECLASSIFICATION/DOWNGRADING SCHEDULE:

16. DISTRIBUTION STATEMENT (of this Report)

This document has been approved for public release, its distribution is unlimited

GRA&I ☑

17. DISTRIBUTION STATEMENT (of the abstract entered in Block 20, if different from Report)

Distribution/ Availability Codes Avail and/or Special A-1

18. SUPPLEMENTARY NOTES

19. KEY WORDS (Continue on reverse side if necessary and identify by block number)

Ostwald ripening (coarsening), aluminum-iron cerium alloy, aluminum-zirconium-vanadium alloy, iron-molybdenum-vanadium alloy, aluminum-molybdenum-vanadium alloy

DTIC COPY INSPECTED

20. ABSTRACT (Continue on reverse side if necessary and identify by block number)

High temperature alloys in order to maintain their strength during long time exposure at high temperatures must have stable microstructures. The dispersed phase coarsening rates in the Al-7.5Fe-3.5Ce and Al-10Fe-1.5Mo-1V alloys, developed for high temperature applications, were compared at 475 and 575°C. To the extent that the average intercept length cubed, $\bar{L}^3$, is a linear function of time during isothermal aging, after an initial transient, the particle coarsening obeys the Lifshitz-Slyozov-Wagner theory. The interfacial energies estimated from the coarsening rates using the theory of particle coarsening show that the

DD FORM 1 JAN 73 1473 EDITION OF 1 NOV 65 IS OBSOLETE

UNCLASSIFIED

SECURITY CLASSIFICATION OF THIS PAGE (When Data Entered)

20. continued

interfaces between the particles and matrix are high energy incoherent interfaces. The dispersed particles in the Al-10Fe-1.5Mo-1V alloy coarsen faster at both temperatures than the particles in the Al-7.5Fe-3.5Ce showing that the latter alloy is more stable at these temperatures.

Since the diffusion in diffusion controlled coarsening usually occurs by a vacancy mechanism, plastic deformation should increase the rate of particle coarsening since plastic deformation increases the vacancy concentration. This has been confirmed in combined creep and coarsening studies with the Al-7.5Fe-3.5Ce alloy.

In order to develop a dispersed phase for high temperature aluminum alloys with lower interfacial energy with the aluminum matrix, chemical modification of Al_3Zr has been investigated. $Al_3(V_{0.875}Zr_{0.125})$ was shown to have substantially less mismatch with aluminum than Al_3Zr resulting in slower coarsening rates. Also, the metastable cubic form of Al_3Zr which is used for grain refinement in 7050 Al alloys persists for longer aging times in $Al_3(V_{0.875}Zr_{0.125})$ than in Al_3Zr.

Introduction

The objective of this research is to provide basic data needed to design a high temperature aluminum base alloy useful to 375° C.

According to the Wagner-Lifshitz-Slyozov (W-L-S) theory for diffusion controlled coarsening of a dispersed phase the average radius at time t, $\bar{r}_t^3$ is proportional to $(\sigma D C_o t)$ where σ is the interfacial energy, D is the diffusivity of the rate controlling element, and C_o is the solubility limit. For microstructural stability at high temperatures, the dispersed phase must be thermodynamically stable, and the product $\sigma D C_o$ must be small. Thus information about σ, D, and C_o are needed as the basis for design of Al alloys for elevated temperature use. If D and C_o are known, then measurement of $\bar{r}_t$ vs. t at constant temperature gives σ. Low values of σ are expected when there is good lattice matching across the interface between dispersed phase and matrix.

Another important consideration is the stability of the microstructure under fatigue loading conditions. Cyclic plastic deformation generates vacancies which amplify the diffusivity. Since D is proportional to $(C_v e^{-q_m/kT})$ where C_v is the vacancy concentration, q_m is the motion energy of vacancy-atom exchange, k is the Boltzmann constant and T is the absolute temperature, even a factor of 2 or 3 increase in the vacancy concentration should have a profound effect on the microstructure.

During the past year the following topics were under study:

1. Al-Fe-Ce alloy. Further work was done on characterizing the dispersed phase in this alloy. Creep studies were begun and the particle coarsening during creep was determined and compared with the particle sizes in the absence of an applied load at the same time and temperature.

2. Al-Al_3X alloys. Additional compositions were investigated seeking better lattice matching between the Al and Al_3X. The best matching was obtained with $Al_3(V_{.875}Zr_{.125})$. Dilute supersaturated solid solutions of Al_3Zr in Al and $Al_3(V_{.875}Zr_{.125})$ in Al were prepared by arc melting. Precipitation and coarsening of the precipitates were studied in this alloy.

3. Al-Fe-Mo-V alloy. The dispersed phases were characterized and the coarsening rate of the stable phase was measured at 475 and 575°C and compared to Al-Fe-Ce.

1. Studies of Al-Fe-Ce Alloy

1.1. Identification of the dispersed second phase in the Alcoa Al-Fe-Ce alloy

X-ray diffraction study of pieces of the forged Al-7.5 wt.% Fe-3.4 wt.% Ce material aged at 475 and 575° C for varied lengths of time indicated that the same dispersed phase(s) is (are) present in the matrix after aging at either temperature. These peaks could not be attributed to the Al_3Fe or Al_8Fe phase. According to the phase diagram of Zarechnyuk (1), the composition of the alloy lies in the Al-Al_3Fe-$Al_{10}Fe_2Ce$ triangle, as shown in Fig. 1. He suggested that $Al_{10}Fe_2Ce$ is body centered tetragonal but was not able to solve the structure. Thus lattice parameters are not yet available.

To find the characteristic diffraction lines of the $Al_{10}Fe_2Ce$ intermetallics for comparison with the diffraction information obtained in the aged alloy, an alloy whose composition is designated by (1) in Fig. 1 was prepared by arc melting small pieces of a casting whose nominal composition is $Al_{10}Fe_2Ce$ with the necessary quantities of Al and Fe. The casting actually contained three phases.

While Fig. 1 shows the nominal composition of alloy 1, the actual composition may be somewhat depleted in cerium. The arc melted button was annealed 24 hours at 500° C in argon, water quenched, and then a diffractometer scan of a polished surface was taken. The diffraction peaks of alloy 1 are compared with those in the 475 or 575° C aged Alcoa Al-Fe-Ce alloy in Table 1 after eliminating the Al peaks. Common diffraction peaks in both specimens attributable to $Al_{10}Fe_2Ce$ are indicated. The diffraction data gives partial confirmation for the phase diagram of Zarechnyuk et al. (1) and indicates that the second phase in the Alcoa Al-Fe-Ce alloy may be his $Al_{10}Fe_2Ce$ phase. The d-spacings of alloy 1 which do not appear to match d-spacings of the aged Alcoa Al-Fe-Ce alloy mostly correspond well with the d-spacings for $FeAl_3$ (2). The weak 5.43 and 5.12Å peaks observed in the Alcoa Al-Fe-Ce,

Table 1. Interplanar spacings and relative intensities obtained in x-ray diffraction study of the RSP P/M Al-Fe-Ce alloy aged at 475 and 575°C and of specimen 1. Aluminum peaks have been subtracted from both.

Aged RSP P/M Al-Fe-Ce Alloy			Specimen 1		
d(A)		I/I_o	d(A)		I/I_o
5.43		10	5.03		<10
5.12		15	4.45	$Al_{10}Fe_2Ce$	<10
4.46	$Al_{10}Fe_2Ce$	15	4.05	$Al_{10}Fe_2Ce$, Al_3Fe	20
4.05	Al_3Fe, $Al_{10}Fe_2Ce$	10	3.98		15
3.96	Al_3Fe, $Al_{10}Fe_2Ce$	10	3.95	$Al_{10}Fe_2Ce$, Al_3Fe	20
3.77	$Al_{10}Fe_2Ce$	<10	3.87		<10
3.67	$Al_{10}Fe_2Ce$, Al_3Fe	<10	3.76	$Al_{10}Fe_2Ce$	<10
3.48		<10	3.69	$Al_{10}Fe_2Ce$, Al_3Fe	10
3.27	$Al_{10}Fe_2Ce$, Al_3Fe	<10	3.54	Al_3Fe	<10
3.20	$Al_{10}Fe_2Ce$	<10	3.34	Al_3Fe	<10
3.17	$Al_{10}Fe_2Ce$	<10	3.26	Al_3Fe, $Al_{10}Fe_2Ce$	10
3.01		<10	3.19	$Al_{10}Fe_2Ce$	15
2.88		<10	3.17	$Al_{10}Fe_2Ce$	15
2.77	$Al_{10}Fe_2Ce$	<10	2.76	$Al_{10}Fe_2Ce$	<10
2.75	$Al_{10}Fe_2Ce$	10	2.66		25
2.61	$Al_{10}Fe_2Ce$	30	2.63		35
2.43	$Al_{10}Fe_2Ce$	25	2.60	$Al_{10}Fe_2Ce$	15
2.27		10	2.56		<10
2.25	$Al_{10}Fe_2Ce$, Al_3Fe	85	2.53	Al_3Fe	<10
2.23	$Al_{10}Fe_2Ce$, Al_3Fe	100	2.47	Al_3Fe	<10
2.10	$Al_{10}Fe_2Ce$, Al_3Fe	70	2.43	$Al_{10}Fe_2Ce$	10
2.05	$Al_{10}Fe_2Ce$, Al_3Fe	<10	2.25	Al_3Fe, $Al_{10}Fe_2Ce$	40
1.60	$Al_{10}Fe_2Ce$	<10	2.23	Al_3Fe, $Al_{10}Fe_2Ce$	40
1.58	$Al_{10}Fe_2Ce$	30	2.17	Al_3Fe	10
1.30	$Al_{10}Fe_2Ce$, Al_3Fe	<10	2.10	Al_3Fe, $Al_{10}Fe_2Ce$	100
			2.04	Al_3Fe, $Al_{10}Fe_2Ce$	80
			2.01	Al_3Fe	10
			1.99	Al_3Fe	10
			1.83		10
			1.59	$Al_{10}Fe_2Ce$	<10
			1.48		<10
			1.36	Al_3Fe	<10
			1.30	Al_3Fe, $Al_{10}Fe_2Ce$	<10

however, are absent in alloy 1. Thus additional research is required to determine the phase or phases present in the Al-7.5 wt.% Fe-3.4 wt.% Ce alloy.

1.2. The effect of plastic deformation on coarsening in the Al-Fe-Ce alloy

An Al-8.8 wt.% Fe-3.7 wt.% Ce billet was obtained from the Air Force Materials Lab in Dayton which had been prepared from gas atomized powder by cold isostatic pressing, hot isostatic pressing and extrusion. The microstructure of the material, Fig. 2a, is markedly more homogeneous than that of the forged material examined earlier. Additionally, the second phase particles have undergone noticeable coarsening associated with the thermomechanical treatment. Figure 2b, a higher magnification micrograph of the thin foil of Fig. 2a, illustrates that a large number of second phase particles are located along subgrain boundaries. This finding will need to be considered during subsequent analysis of the coarsening kinetics in this material.

Several specimens machined from the extruded material were crept at elevated temperatures. The creep curves of several of these specimens are presented in Figs. 3 through 5. Tests were terminated after 60 hours in cases where fracture had not occurred. The curves do not exhibit well defined regions of secondary creep, as often expected in dispersion strengthened materials. The specimens which fractured exhibited large strains (up to 35%) and ductile cup and cone fractures.

Shadowed two stage replicas of the alloy within the gage section and material just outside the gage section were prepared to examine the effect of creep deformation on the particle size. Figures 6 and 7 illustrate a noticeable enhancement of particle coarsening in the deformed regions. Values for volume fraction of second phase V_v, surface area per unit volume S_v, and particle mean intercept length for deformed and undeformed regions of

several crept specimens are presented in Table 2. An insufficient number of specimens have been crept at this time to construct a plot of intercept length cubed vs. time to conform with the LSW theory predictions, but preliminary calculations of the enhanced vacancy concentrations are included in Table 2. They are in the range 2 to 4.

Table 2. Results of particle size analysis in crept specimens of extruded RSP P/M Al-8.8Fe-3.7Ce alloy.

Creep Conditions	Volume Fraction of Dispersed Phase	Surface Area per Unit Vol. mm^2/mm^3	Mean Intercept Length	Enhancement of Vacancy Concentration, C_σ/C_o
316° C, 4750 psi, 60 hr				
Deformed region	0.23	6340	0.150 μm	3.8
Undeformed region	0.24	9920	0.096 μm	
425° C, 2500 psi, 60 hr				
Deformed region	0.23	3880	0.24 μm	1.7
Undeformed region	0.24	4880	0.20 μm	
425° C, 4750 psi, 0.74 hr				
Deformed region	0.26	5690	0.18 μm	2.65
Undeformed region	0.23	7020	0.13 μm	
375° C, 4750 psi, 43 hr				
Deformed region	0.24	5550	0.17 μm	1.8
Undeformed region	0.24	6760	0.14 μm	
375° C, 10,000 psi, 0.23 hr				
Deformed region	0.20	7560	.107 μm	2.0
Undeformed region	0.19	8880	.085 μm	

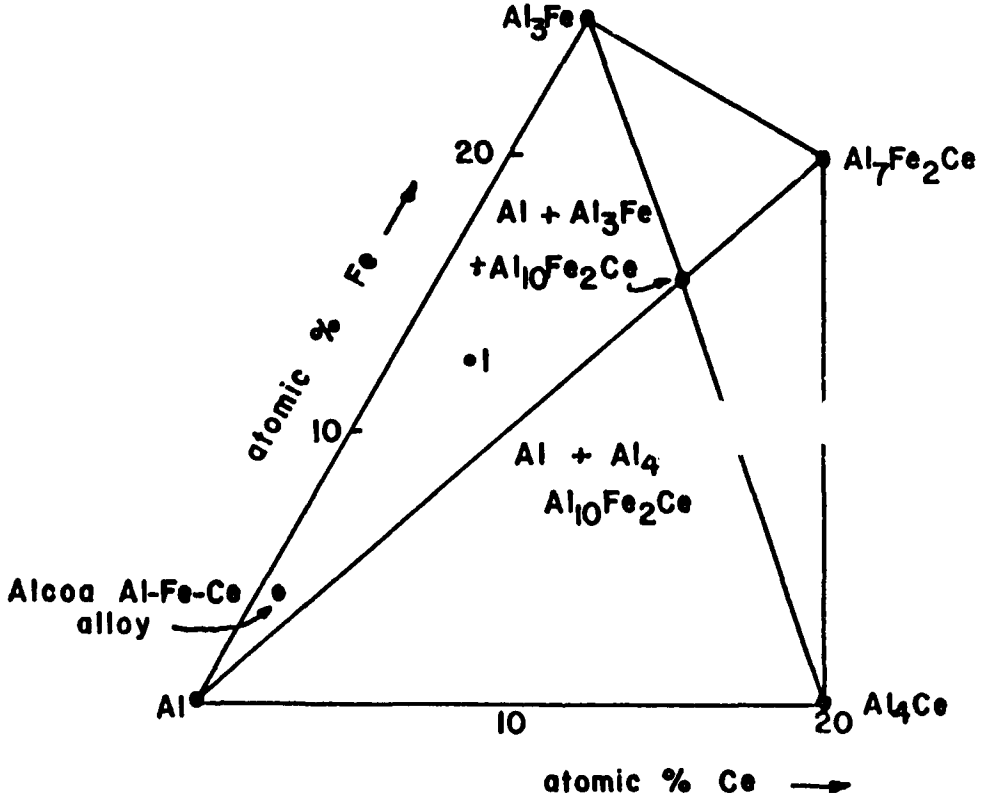

Fig. 1. Al-Fe-Ce phase diagram according to Zarechnyuk (1). 500°C isotherm.

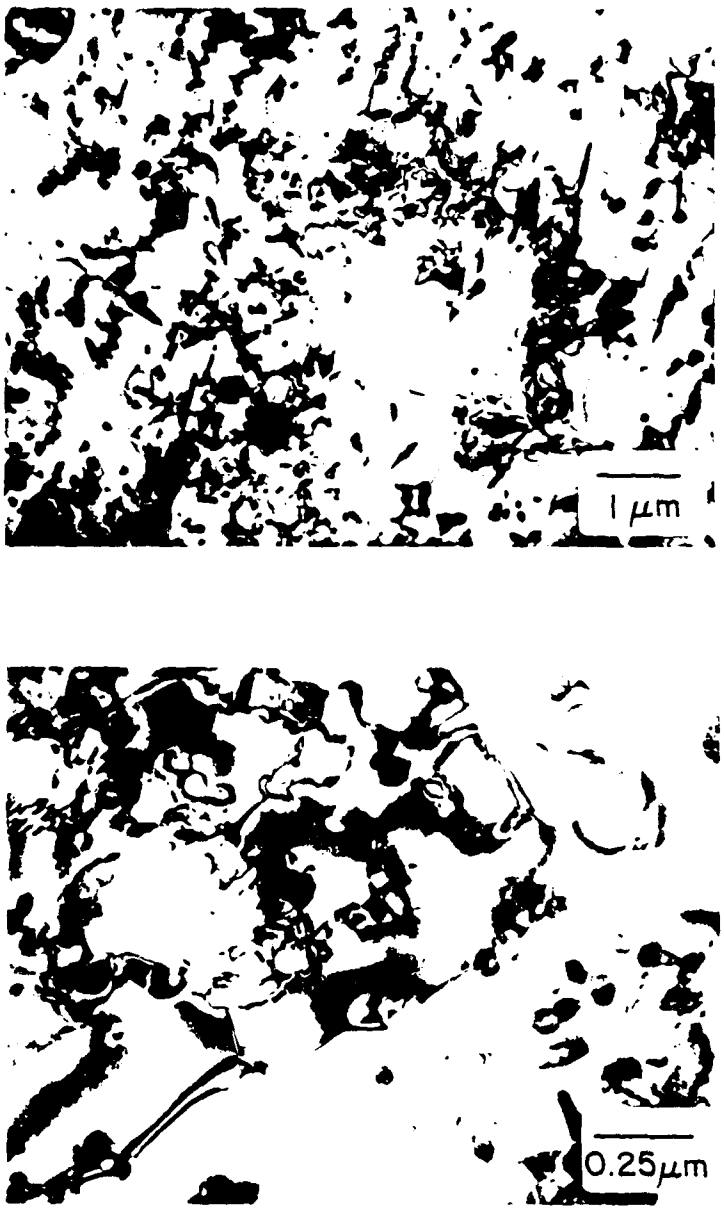

(a)

(b)

Fig. 2. TEM micrographs of thin foils of the Al-8.8Fe-3.7Ce extrusion in the as-received condition. (a) low magnification and (b) high magnification.

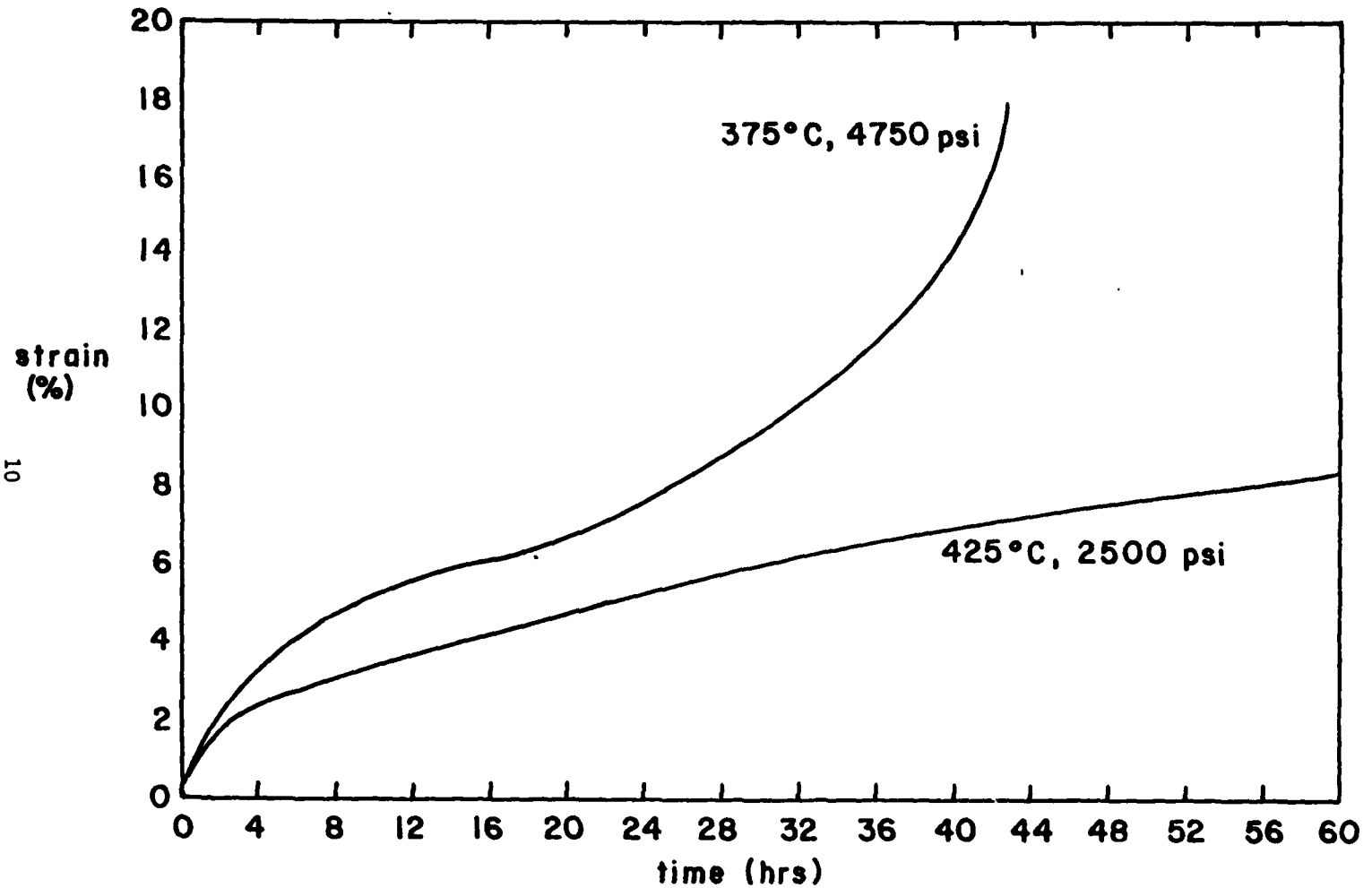

Fig. 3. Strain vs. time curve for extruded Al-Fe-Ce specimens crept at 375°C, 4750 psi and 425°C, 2500 psi.

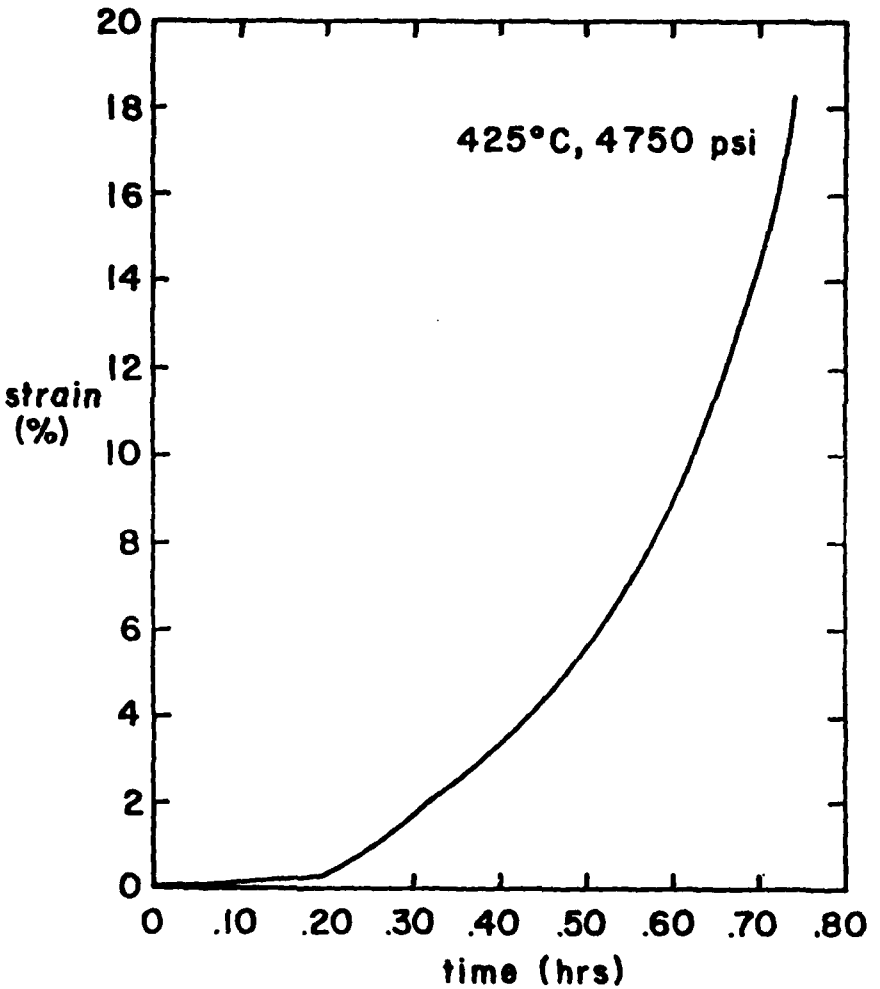

Fig. 4. Strain vs. time curve for extruded Al-Fe-Ce specimen crept at 425°C, 4750 psi.

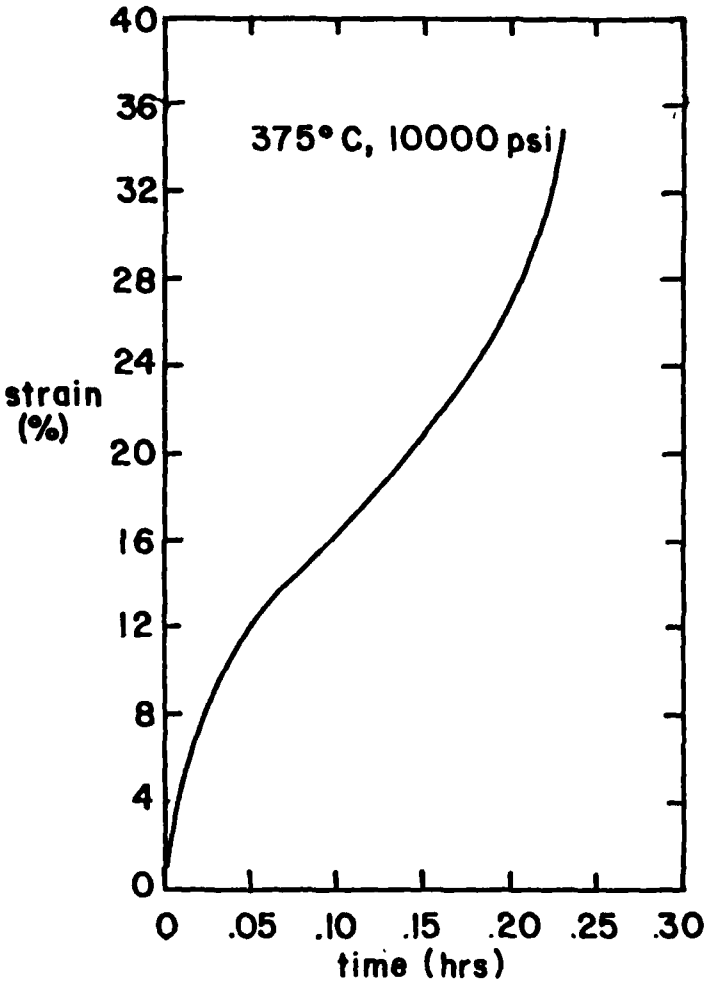

Fig. 5. Strain vs. time curve for extruded Al-Fe-Ce specimen crept at 375°C, 10,000 psi.

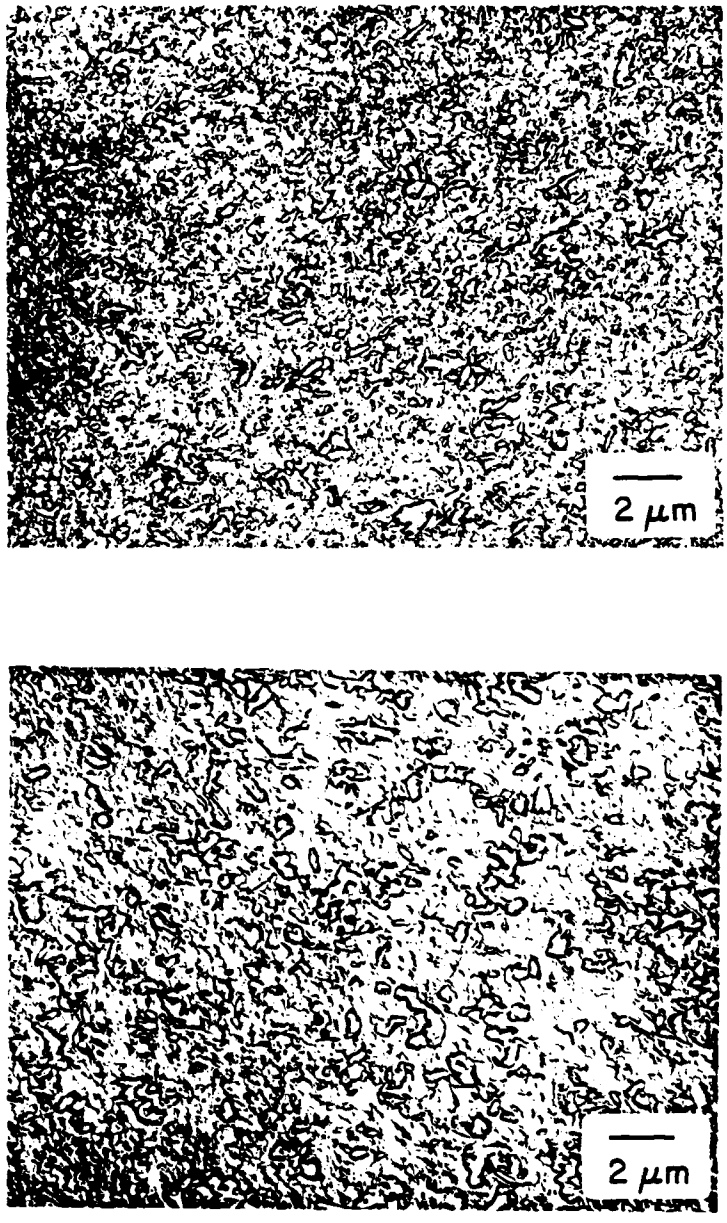

(a)

(b)

Fig. 6. TEM micrographs of replicas of specimen crept at 316°C, 4750 psi in regions (a) away from the gage section and (b) within the gage section.

(a)

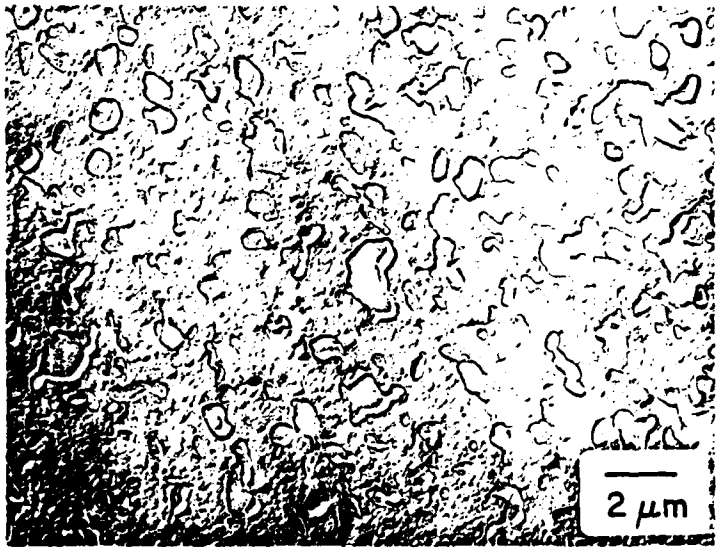

(b)

Fig. 7. TEM micrographs of replicas of specimen crept at 425°C, 2500 psi in regions (a) away from the gage section and (b) within the gage section.

2. Studies of Al Alloys with Al_3X Dispersoids

2.1 Lattice parameters of Al(Ti,V,Zr,Hf)

Because of the similarity between the crystal structures of Al and Al_3X (D_{4h}^{17} space groups) an aluminum based alloy containing suitable Al_3X dispersoid particles may be the basis for a high temperature Al alloy. In order to reduce the interfacial energy and the driving force for particle coarsening, it is desirable to adjust the lattice parameters or Al_3X by varying X.

Table 3 gives crystallographic data on some tetragonal $Al_3(X)$ compounds selected because of their lattice parameter similarity to Al. The two variants DO_{22} and DO_{23} differ by a modulation along their c-axis. Thus, two phase regions exist between DO_{22} and DO_{23} compounds. For Al_3V the lattice parameter, a, is approximately 7% less than a of aluminum; however, the mismatch in the c directions is less than 3%. For both the Al_3Zr and the Al_3Hf the mismatch in the a direction with Al is only 1% while the mismatch along the c axis ranges from 5 to 7%.

In the previous annual report it was shown that matching with Al was better for $Al_3(Ti_{0.75}Zr_{0.25})$ than for either Al_3Ti or Al_3Zr (3). Similarly, $Al_3(Ti_{0.87}Hf_{0.13})$ showed better matching than Al_3Ti or Al_3Hf. The research during the past year was aimed at further improving this matching. Al_3X compounds containing V and additional $Al_3(Hf,Zr,V)$ compositions were investigated.

Experimental Procedures

The method used previously for alloy preparation was followed. Small, approximately 5 grams, Al-2 at.%(Ti,V,Zr,Hf) alloy buttons were made in a gettered argon atmosphere by nonconsumable W arc melting using a water cooled Cu cathode as the crucible. The Al was 99.996% pure, the Ti and V were Johnson-Mathey spectrochemical grade, and the Zr and Hf were cut from crystal

Table 3. Comparison of the lattice parameter of aluminum with numerous $Al_3(X)$ D^{17}_{4h} space group compounds (7)

Compound	Ref.	Structure	Lattice Parameters in nm and Their Ratios			
Al		cubic	a_o=0.40495			
Al_3Ti	2	tet.(DO_{22})	a=0.5443	$a'=a/\sqrt{2}$=0.3849	a'/a_o=0.9505	c=0.8610	$c/2a_o$=1.0641
Al_3V	3	tet.(DO_{22})	a=0.5345	$a'=a/\sqrt{2}$=0.3779	a'/a_o=0.9333	c=0.8322	$c/2a_o$=1.0275
Al_3Zr	4	tet.(DO_{23})	a=0.4013		a/a_o=0.9910	c=1.7321	$c/4a_o$=1.0693
Al_3Hf	5	tet.(DO_{23})	a=0.3989		a/a_o=0.9851	c=1.7155	$c/4a_o$=1.0591

a_o=a(Al), a=a(Al_3X), c=c(Al_3X)

bars prepared by the Van Arkel process, i.e., thermal reduction of iodides. Each button was melted four to five times, and inverted between melting to insure homogeneity, and then annealed for 24 hours at 475° C. The presence of large intermetallic compound particles were verified by optical metallography.

For powder x-ray analysis, the buttons were powdered with an automatic filing machine, and the fraction passing through a 150 mesh screen was used. The specimens were annealed at 330° C for 4 hours to remove any residual stresses incurred during filing and then mixed with Si powder for an x-ray peak position standard. The diffraction data were obtained with Cu-Kα radiation in a Rigaku "Geigerflex" D/max-IIA x-ray diffractometer.

Results and Discussion

Al-V-Zr System

The a and c lattice parameters of $Al_3(Zr_xV_{1-x})$ compared to a_o for the Al(ss) are shown in Figs. 8a and b, respectively. Previous results from the Al-Ti-Zr-Hf system are also included for comparison. The open symbols represent the results of the present alloys while the closed circles are JCPDS data for the Al_3Ti, Al_3V, Al_3Zr and Al_3Hf intermetallic compounds, cards #2-1127(1), #7-399(4), #2-1093(5) and #13-512(6), respectively. The nearly horizontal dashed lines in Figs. 8a, b and the following figures represent the cubic lattice parameter, $a_o(ss)$ and $4a_o(ss)$, respectively, of the Al solid solution measured from the present x-ray data. Since $a_o(ss)$ is very nearly equal to a_o of Al($\Delta a_o(0.1\%)$), one may conclude that virtually all of the Ti, V, Zr and Hf are present in the intermetallic $Al_3(X)$-type compounds. For Al_3Ti and Al_3V, $a/\sqrt{2}$ is plotted rather than a and $2c$ is plotted rather than c for better comparison with c of the $Al_3Zr(ss)$-type compounds (DO_{23}). In all cases, the measured values of a and c for Al_3Ti, Al_3V, Al_3Zr and

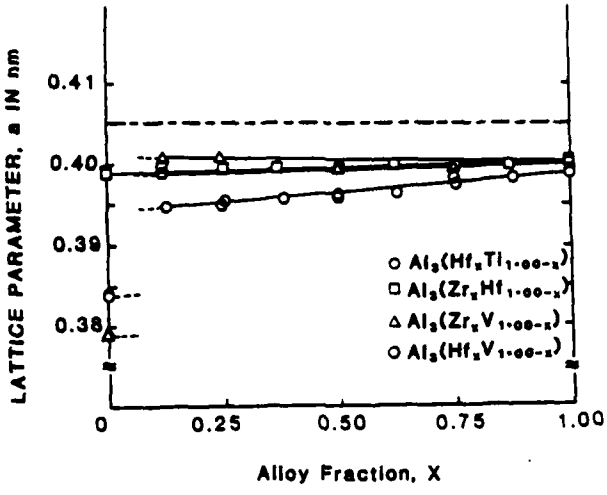

(a)

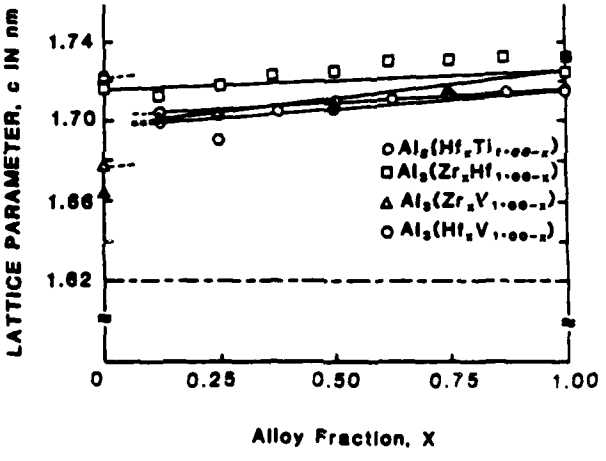

(b)

Fig. 8 Lattice parameters of Al_3Hf-Al_3Ti, Al_3Zr-Al_3Hf, Al_3Zr-Al_3V, Al_3Hf-Al_3V psuedo binary intermetallic compounds contained in Al alloys with 2 at.% solute. The c values of the $Al_3(Ti,V)$-type solid solutions are multiplied by 2 for comparison with the c's of the $Al_3(Zr,Hf)$-type solid solutions: open symbols, present results; closed symbols, JCPDS data. Dashed lines are a_o and $4a_o$ of Al solid solution.

Al_3Hf prepared by arc melting are in good agreement with the JCPDS compiled data.

As mentioned previously, since the structure of Al_3Ti and Al_3V is DO_{22} while the structure of the $Al_3(Zr,Hf)$ is DO_{23}, there must be a two phase region in the psuedo-binary system for each combination of the above DO_{22} and DO_{23} intermetallic compounds. Such was observed in the previous study of the Al_3Ti-Al_3Zr for $Al_3(Zr_xTi_{1-x})$ with x between 0.125 and 0.250; however, for the Al_3V-Al_3Zr the discontinuous region is shifted to between 0 and 0.125 for $Al_3(Zr_xV_{1-x})$.

As previously observed in the Al_3Ti-Al_3Zr system (3), the addition of Ti to $Al_3(Zr_xTi_{1-x})$ increases the lattice mismatch along the a-axis with Al; however, the mismatch between $4a_o$ and c is greatly reduced. This same response is also observed when V is increased in $Al_3(Zr_xV_{1-x})$; however, less change along the a-axes is found in the V containing compounds compared to those with Ti. In the Al-V-Zr system, the compound demonstrating the least average overall lattice mismatch (δ=2.39%) is $Al_3(V_{0.875}Zr_{0.125})$. Here,

$$\delta = \frac{100}{3}\left[\frac{2(1-a(Al_3X)}{a(Al)} + \frac{C(Al_3X)}{4a(Al)}\right] .$$

Al-V-Hf System

Similar to the above, data for $Al_3(Hf_xV_{1-x})$ are also presented in Figs. 8a and b. Once again, no detectable solid solubility of V or Hf in Al was found. Similarly, a two phase field was found to exist for $Al_3(Hf_xV_{1-x})$ between x = 0 and 0.125. The alloy demonstrating the least average overall lattice mismatch was $Al(V_{0.875}Hf_{0.125})$ where δ = 2.69%.

Al-Ti-Zr-Hf System

Numerous quaternary compounds in the general system $Al_3(Ti,V,Zr,Hf)$ were

then investigated to further characterize the lattice parameter variation near the discontinuous region. The results for the $Al_3(Ti_{0.75}Zr_xHf_{0.25-x})$ and $Al_3(Ti_{0.875}Zr_xHf_{0.125-x})$ intermetallic compounds are shown in Figs. 9a,b and 10a,b, respectively. As expected, Vegard's law is obeyed between combinations of psuedo-binary compounds with identical crystal structures. Furthermore, the addition of Hf to the Al_3Ti-Al_3Zr system acts to shift the discontinuous region of the lattice variation towards x = 0.125. The compound giving the minimum mismatch is $Al_3(Ti_{0.875}Zr_{0.109375}Hf_{0.015625})$ with δ=2.70%.

Al-V-Zr-Hf System

The a and c lattice parameters for the psuedo-ternary $Al_3(V_{0.875}Zr_xHf_{0.125-x})$ compounds are shown in Figs. 10a and b, respectively. Here only the DO_{23} edge of the two phase field was investigated. Again Vegard's law was rather closely followed.

Al-Ti-V-Zr System

Along these same lines, the variation in lattice parameters a and c for $Al_3(Ti_xV_{0.75-x}Zr_{0.25})$ are shown in Figs. 11a and b, respectively. It was hoped that the addition of V, replacing Ti, would promote an improved mismatch along the c-axis while maintaining a nearly equivalent mismatch along the a-axis (see Table 1). However, this was not the case.

Similarly as in the Al-Ti-Zr-Hf system, a psuedo-ternary phase diagram of the Al_3V-Al_3Zr-Al_3Hf system is presented in Fig. 12. Since all the alloys were annealed at 475°C, the diagrams probably apply for this temperature. The extents of stability of the DO_{22} and DO_{23} phases are shown along with the approximate location of the two phase fields, i.e., the designation Al_3V(ss) refers to a solid solution having the DO_{22} crystal structure while Al_3(Zr,Hf)(ss) refers to a solid solution having the DO_{23} structure.

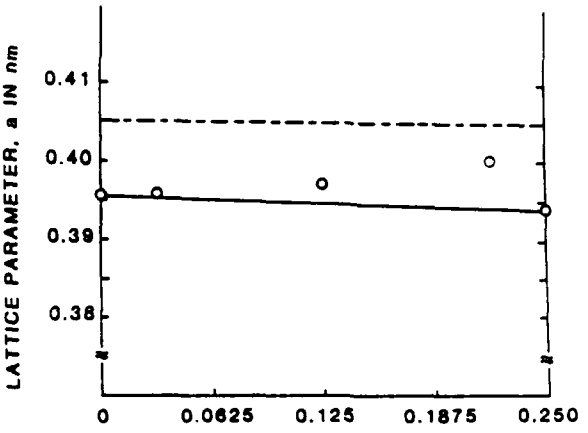

(a)

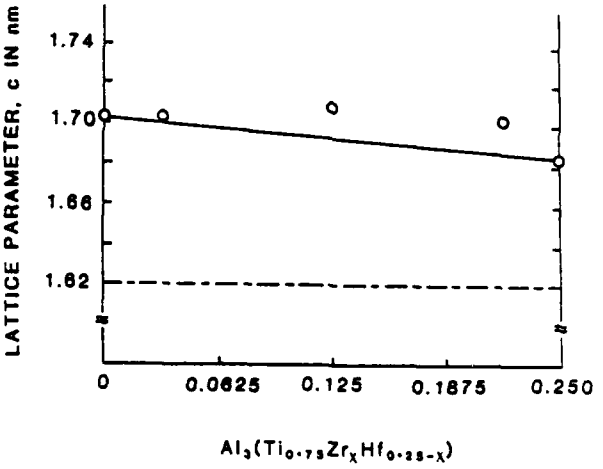

(b)

Fig. 9. Lattice parameters of $Al_3(Ti_{0.75}Zr_xHf_{0.25-x})$ versus x in Al-2 at.% (Ti,Zr,Hf) alloys. Dashed lines are a_o and $4a_o$ of Al solid solutions.

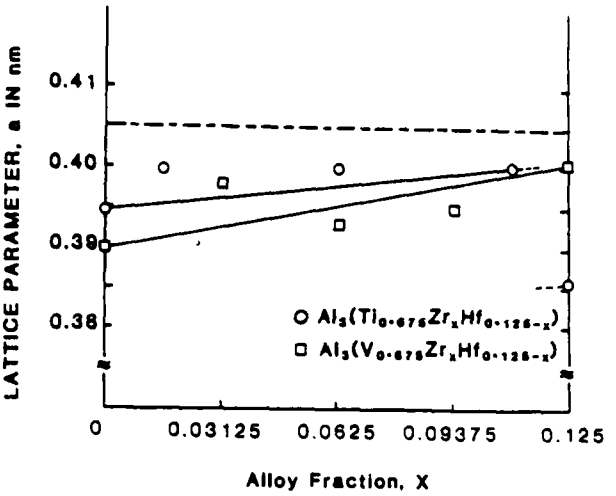

(a)

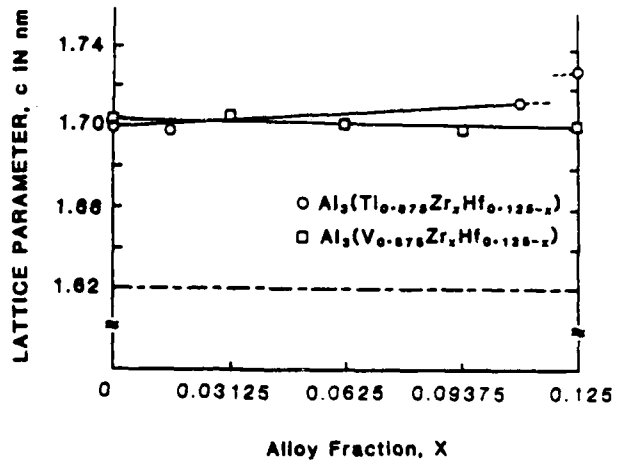

(b)

Fig. 10. Lattice parameters of $Al_3(Ti_{0.875}Zr_xHf_{0.125-x})$ and $Al_3(V_{0.875}Zr_xHf_{0.125-x})$ versus x in Al-2 at.% (Ti, V,Zr,Hf) alloys. The c values of the Al_3(Ti,V)-type solid solutions are multiplied by 2 for comparison with the c's of the Al_3(Zr,Hf)-type solid solutions. Dashed lines are a_o and $4a_o$ of the Al solid solutions.

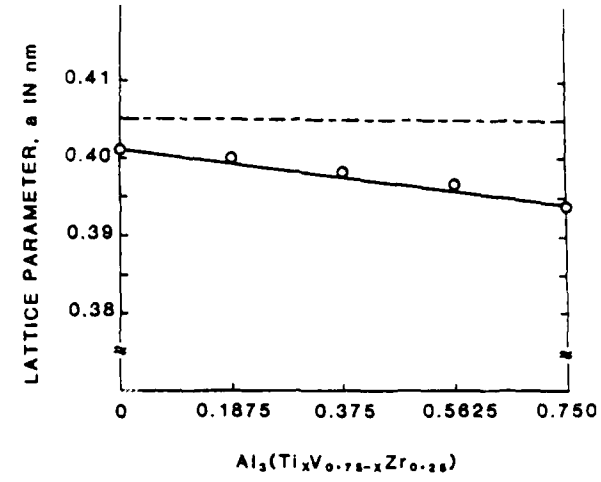

(a)

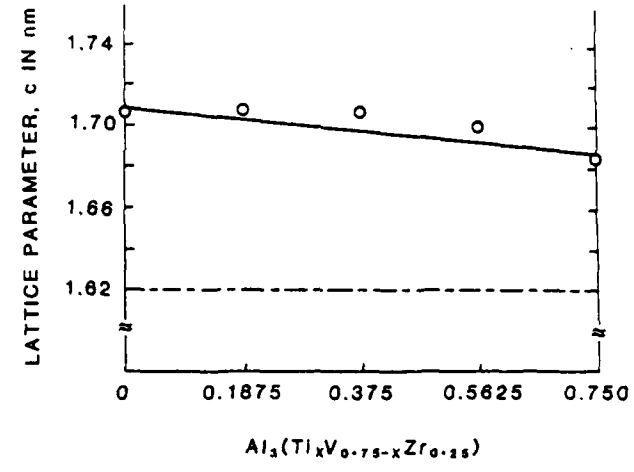

(b)

Fig. 11. Lattice parameters of $Al_3(Ti_xV_{0.75-x}Zr_{0.25})$ versus x in Al-2 at.% (Ti,V,Zr) alloys. Dashed lines are a_o and $4a_o$ of the Al solid solutions.

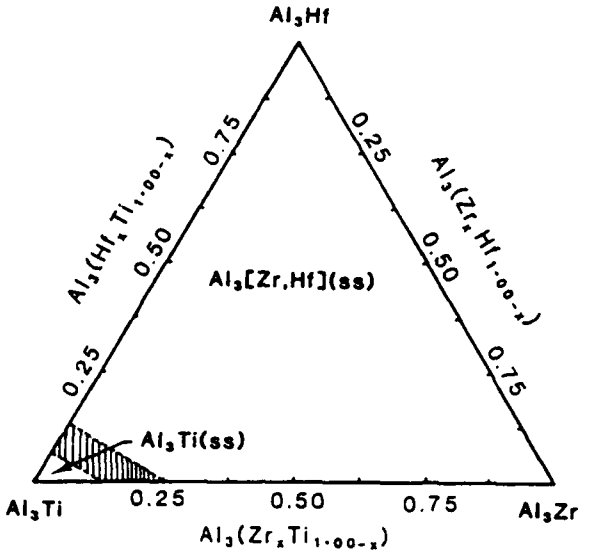

(a)

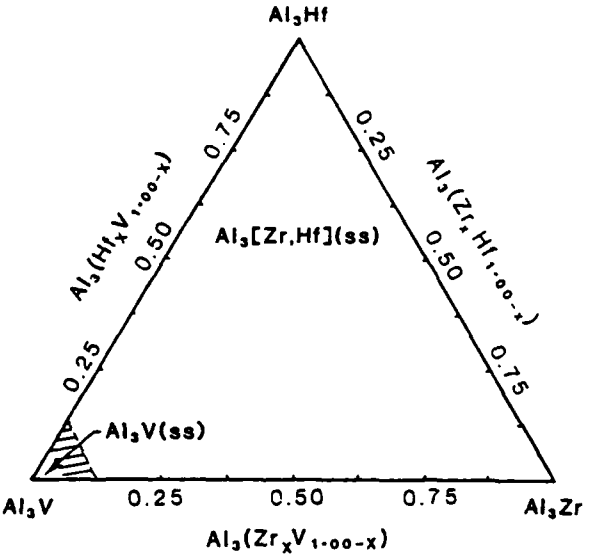

(b)

Fig. 12. Psuedo-ternary Al_3Ti-Al_3Zr-Al_3Hf and Al_3V-Al_3Zr-Al_3Hf phase diagrams constructed from x-ray data of alloys homogenized at 475° C for 24 hours. The shaded region represents the compound solid solution.

As shown in the Al-Ti-Zr-Hf system, while the addition of V to Al_3Zr or Al_3Hf increases the mismatch of the a lattice parameter with a_o for the Al(ss), the mismatch of c with $4a_o$ of the Al(ss) is improved. Once again, the least mismatch for V in Al_3V-Al_3Zr or Al_3V-Al_3Hf occurs with the maximum V allowable without forming the DO_{22} crystal structure, e.g., $Al_3(Ti,V)$ phase. In spite of the fact that c for Al_3Hf matches $4a_o$ of the Al(ss) better than Al_3Zr, V has a larger effect on c of Al_3Zr so the least average overall lattice mismatch occurs in this system.

From the average overall lattice mismatch point of view, the most promising intermetallic compounds for possible elevated temperature applications are presented in Table 4.

Table 4. $Al_3(Ti,V,Zr,Hf)$ intermetallic compounds demonstrating minimum average overall lattice mismatch

Intermetallic Compound	Average Overall Lattice Mismatch (δ)
Al_3Zr	2.88%
$Al_3(V_{0.875}Zr_{0.125})$	2.39%
$Al_3(V_{0.875}Hf_{0.125})$	2.69%
$Al_3(Ti_{0.875}Zr_{0.109375}Hf_{0.015625})$	2.70%

2.2. Precipitation characterization during the decomposition of hyperperitectic Al-Zr and Al-V-Zr alloys

To evaluate the effect of lattice mismatch between the intermetallic particle and the Al matrix on particle coarsening kinetics, the precipitation sequences in some of the more promising alloys previously presented in Table 4 were determined. In the past, numerous attempts have been made to characterize the decomposition of both sub- and hyperperitectic Al-Zr alloys (8-13). In general, the precipitation sequence is commonly given by

Solid Solution → Cubic Al_3Zr (rods & spheres) → Tetragonal Al_3Zr .

Experimental

Small, approximately 3.5 gram, Al-0.35 wt.% Zr and Al-0.40 wt.% V-0.10 wt.% Zr alloy buttons were made in a gettered argon atmosphere by nonconsumable W arc melting using a water cooled Cu cathode as the crucible. The large copper volume ensured very rapid solidification ($\sim 10^{2}$ °K/sec) which resulted in the formation of a supersaturated solid solution. The Al was 99.996% pure; the V was Johnson-Mathey spectrochemical grade, and the Zr was cut from crystal bars prepared by the Van Arkel process. Each button was melted four to five times and inverted between melting to insure honogeneity.

The buttons were initially cold rolled 95% to enhance precipitation in the as cast, supersaturated solid solution. Isothermal aging was performed in a vacuum furnace (10^{-6} torr) for periods ranging from 0.5 hours to 150 hours or until the equilibrium tetragonal phase formed. Thin foils for TEM were prepared by electropolishing in a solution of 80% methanol-20% perchloric acid at 150V and at less than -70° C. The foils were examined in a Hitachi H-700H STEM microscope.

Observations

Al-0.35 wt.% Zr

Neither optical nor electron microscopy revealed the presence of any particles in the as-cast structure. The first indication of decomposition from the supersaturated solid solution was observed after 0.5 hours at 450° C. Small, approximately 20 nm, spherical particles appeared throughout the matrix in a rather inhomogeneous distribution (Fig. 13). With continued aging, no significant change in average particle size was noted; however, the density of particles increased. Electron diffraction from such particles showed them to be cubic (LI_2) with nearly the lattice parameter of the Al matrix. Similar structures have been observed by other workers in both sub- and

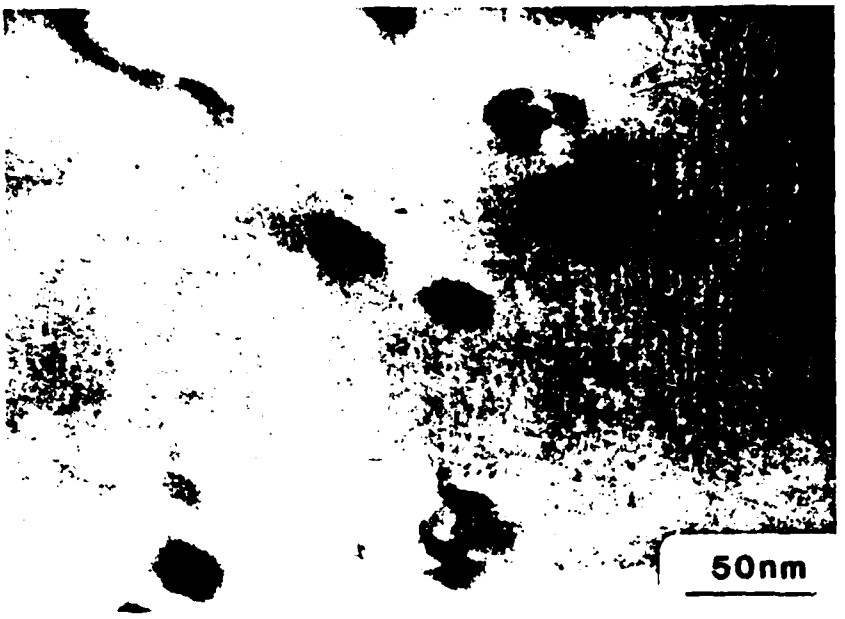

Fig. 13. Bright field micrograph of Al_3Zr particles in Al matrix after isothermal aging of 0.5 hrs. at 450° C.

Fig. 14. Weak bean, dark field micrograph of Al_3Zr rods intermixed with spherical particles after isothermal aging of 13.5 hrs. at 450° C.

hyperperitectic Al-Zr alloys (6-12).

With continued aging the spherical particles appeared to align themselves along preferred directions: ⟨100⟩, ⟨110⟩ and ⟨111⟩. It was not until 13.5 hours that rods, aligned along similar directions, intermixed with spherical particles were observed (Fig. 14). Numerous models have been proposed to explain the formation of these rods; however high magnification micrographs (Fig. 15) support the model proposed by Nes (11). Here, precipitation on a dislocation associated with helical climb may explain the appearance of long rod-shaped precipitates. After 20 hours of aging, surface energy apparently drives these rods to thin down locally and pinch off (Fig. 16), ultimately forming the equilibrium tetragonal phase (Fig. 17). Similarly, these equilibrium particles are oriented along ⟨100⟩, ⟨110⟩, and ⟨111⟩ directions. As expected, the equilibrium shape appears platelike with faceted caps.

Al-0.40 wt.% V-0.10 wt.% Zr

Once again, neither optical nor electron microscopy revealed the presence of precipitates in the as-cast structure. In fact it was not until 1 hour of aging at 450° C that small (~ 10 nm) spherical particles were observed (Fig. 18). The decomposition sequence was identical to that observed in the Al-0.35 wt.% Zr alloy; however, the kinetics were appreciably slower. For instance, rod-shaped precipitates were not observed until after 50 hrs. of aging at 450° C as compared to 13.5 hrs. in the Al-Zr alloy (Fig. 19). Similarly, the equilibrium, tetragonal phase was not prevalent until after 100 hrs. of aging as compared to 20 hrs. in the previous system (Fig. 20). This deceleration in kinetics is attributed to the improved lattice matching for the $Al_3(V_{0.875}Zr_{0.125})$ phase. Furthermore, the shape of the equilibrium phase no longer exhibits faceted caps as previously found for the Al_3Zr phase.

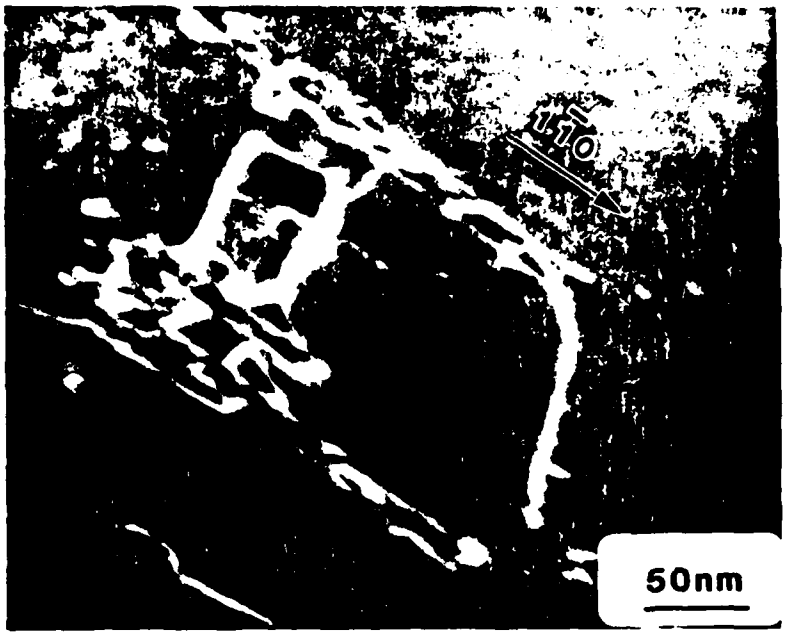

Fig. 15. Precipitation of Al_3Zr rod on a dislocation associated with helical climb. 15 hrs. at 450° C.

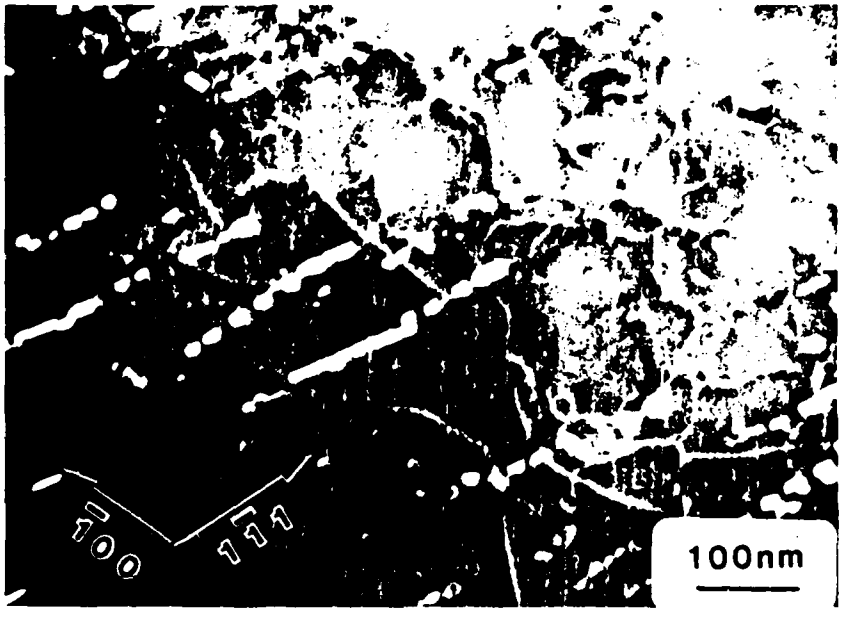

Fig. 16. After 20 hrs. at 450° C, rod shaped particles are apparently driven to thin and pinch off as shown by this micrograph. Electron diffraction patterns indicate the particles are now tetragonal.

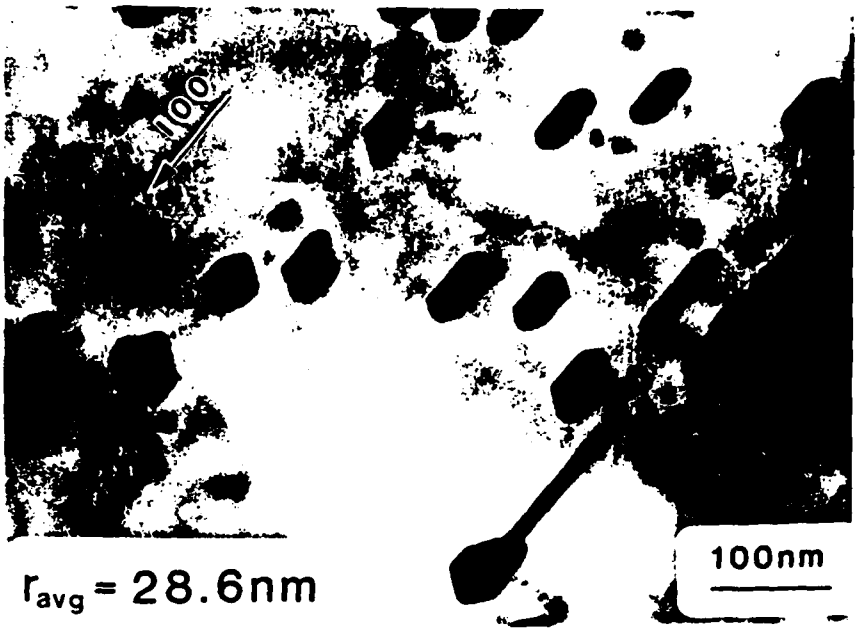

Fig. 17. Equilibrium tetragonal Al_3Zr phase after 20 hrs. isothermal aging at 450°C.

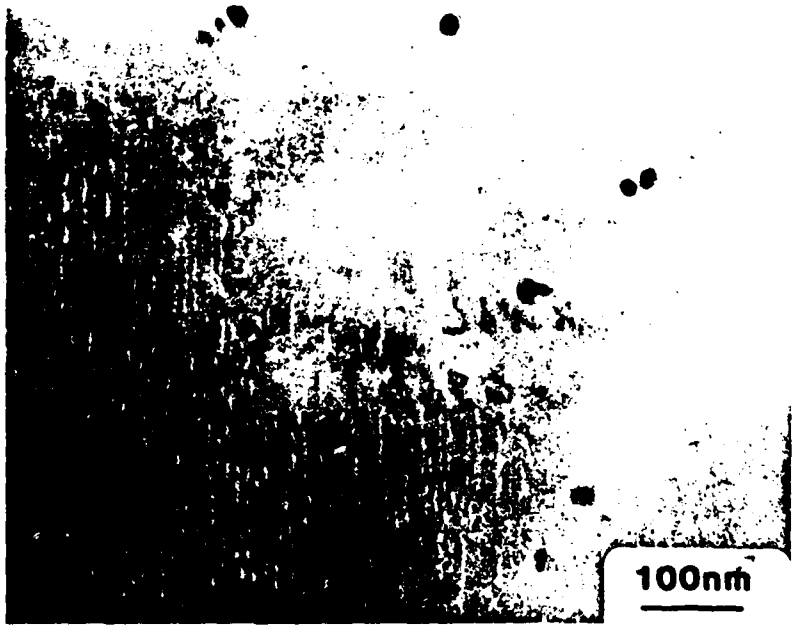

Fig. 18. Bright field micrograph of spherical $Al_3(V_{0.875}Zr_{0.125})$ particles after 1 hr. at 450°C.

Fig. 19. Weak beam, dark field micrograph of cubic rod shaped particles after isothermal aging for 50 hrs. at 450° C.

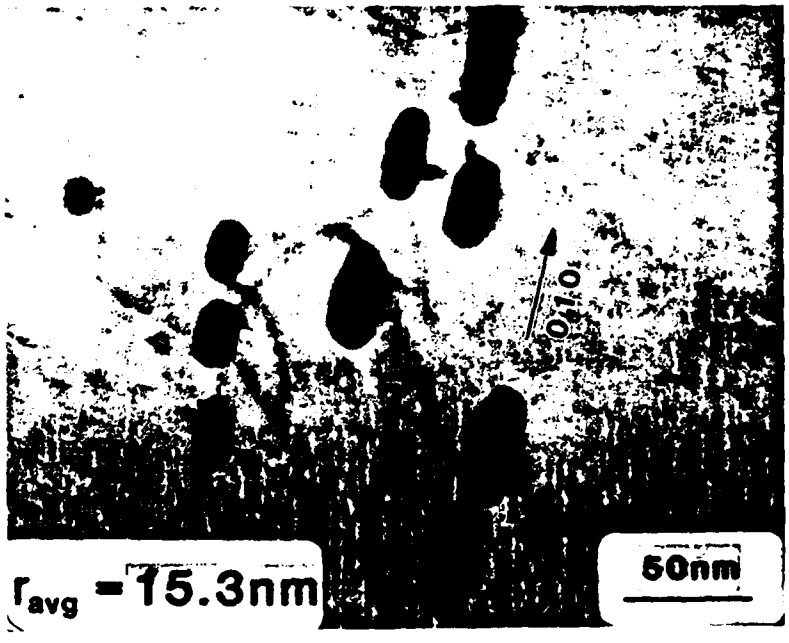

Fig. 20. Bright field micrograph of equilibrium tetragonal $Al_3(V_{0.875}Zr_{0.125})$ phase after 100 hrs. at 450° C.

These plate-shaped particles with hemispherical caps were present even after 150 hours of aging.

The improved lattice matching between the equilibrium precipitate and the matrix affects the shape as well as stabilizing the cubic phase. Thus Al with $Al_3(V_{0.875}Zr_{0.125})$ dispersoids shows promise for further study as the basis for a high temperature aluminum alloy. In addition, cubic Al_3Zr is used as a grain refiner in commercial Al alloys such as alloy 7050. Since cubic $Al_3(V_{0.875}Zr_{0.125})$ is more stable, there may be some advantages in using it for grain refinement.

3. Studies of Al-Fe-Mo-V Alloy

For comparison with the Al-Fe-Ce alloy developed by Alcoa, study of the microstructural stability of the Al-Fe-Mo-V alloy developed by Pratt and Whitney was undertaken. A small amount of an Al-10 w/o Fe-1.5 w/o Mo-1 w/o V alloy was obtained from AFML in the form of halves of two broken tensile specimens.

From x-ray diffraction of the as-received material, the main second phase was "$FeAl_6$" (14,15). During aging for 5 hours at 475°C almost all of the dispersed phase was converted to "$FeAl_3$ (16). Table 5 lists the x-ray lines and their identification for an as-received sample and for a sample aged 10 hours at 575°C. Presumably, some of the Mo and V have entered the dispersed phase so $FeAl_6$ and $FeAl_3$ are nominal compositions.

Figure 21 shows the decrease in microhardness at room temperature from aging at 475 and 575°C due to conversion of the $FeAl_6$ to $FeAl_3$ and coarsening of the $FeAl_3$. As expected, the hardness decreases more rapidly at 575 than at 475°C.

The microstructures of the Al-10Fe-1.5Mo-V alloy as-received and aged 10 hours at 575°C are compared in Fig. 22a and b which are transmission electron micrographs of thin foils. Rather large plate-shaped "Al_6Fe" particles are clearly seen in the as-received sample. Smaller particles are also present. During aging for 10 hours at 575°C, there was considerable grain growth. The particles now "Al_3Fe" are more equiaxed.

Using quantitative metallographic procedures identical to those used previously for the Al-Fe-Ce alloy, the surface area of dispersed phase per unit volume S_v and the volume fraction of the dispersed phase V_v were measured. The mean intercept length $\bar{L}$ is $4V_v/S_v$. V_v was approximately 20 vol.%.

Table 5. Principal X-ray Diffraction Peaks
Al-10Fe-1.5Mo-1V

a. As-received

d(Å)	Measured Intensity	Structure and Reflection Plane
4.87	medium	$FeAl_6$ (110)
4.385	medium	$FeAl_6$ (002)
4.26	weak	$FeAl_6$ (111)
3.715	weak	$FeAl_6$ (020)
3.27	medium	$FeAl_6$ (112)
2.84	weak	$FeAl_6$ (022)
2.58	v. strong	$FeAl_6$ (202)
2.51	medium	$FeAl_6$ (113)
2.33	v.v. strong	Al(111), $FeAl_6$ (130)
2.24	m. strong	$FeAl_6$ (131)
2.20	medium	$FeAl_6$ (004)
2.17	strong	$FeAl_6$ (203)
2.14	strong	$FeAl_6$ (222)
2.07	weak	$FeAl_6$ (310)
2.05	strong	$FeAl_6$ (132)
2.02	v.v. strong	Al(200), $FeAl_6$ (311)
1.88	v. weak	$FeAl_6$ (312), (223), (024)
1.86	weak	$FeAl_6$ (040)
1.82	v. weak	$FeAl_6$ (041), (204), (133)
1.47	v. weak	$FeAl_6$ (421), (006)
1.43	m. strong	Al(220), $FeAl_6$ (151), (225), (333)
1.31	v. weak	$FeAl_6$ (404), (334)
1.29	medium	$FeAl_6$ (244), (153)

b. Aged at 575°C for 10 hours

d(Å)	Measured Intensity	Structure and Reflection Plane
4.27	weak	$FeAl_3$ (112)
4.03	medium	$FeAl_3$ (020)
3.95	medium	$FeAl_3$ (003)
3.67	medium	$FeAl_3$ (311)
3.53	strong	$FeAl_3$ (220)
3.33	medium	$FeAl_3$ (022)
3.25	medium	$FeAl_3$ (113), (401)
3.07	m. strong	$FeAl_3$ (312)
2.58	v. strong	$FeAl_3$ (313)
2.52	v. weak	$FeAl_3$ (421)
2.455	v. weak	$FeAl_3$ (600)
2.38	v. strong	$FeAl_3$ (024), (005), (132)
2.33	v.v. strong	Al(111)
2.24	weak	$FeAl_3$ (331)
2.18	strong	$FeAl_3$ (314)
2.09	strong	$FeAl_3$ (205), (332), (620)
2.08	m. strong	$FeAl_3$ (205)
2.04	medium	$FeAl_3$ (710), (423), (025)
2.02	v.v. strong	Al(200), $FeAl_3$ (513), (040), (404)
1.93	weak	$FeAl_3$ (134)
1.89	weak	$FeAl_3$ (315)
1.86	weak	$FeAl_3$ (225), (603)

a. L. K. Walford, Acta. Cryst. 18 (1965) 287.

b. P. J. Black, Acta. Cryst. 8 (1955) 43.

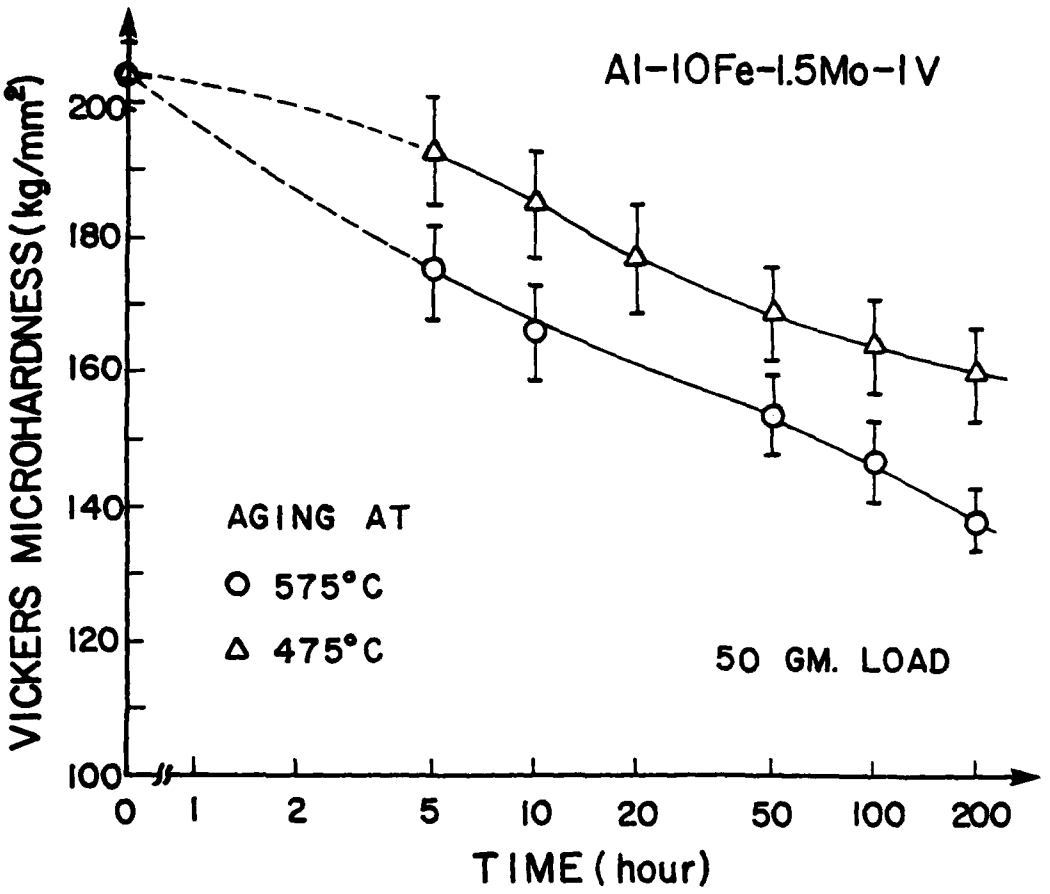

Fig. 21. Microhardness of RSP Al-10Fe-1.5Mo-1V alloy versus coarsening time at 475 and 575° C.

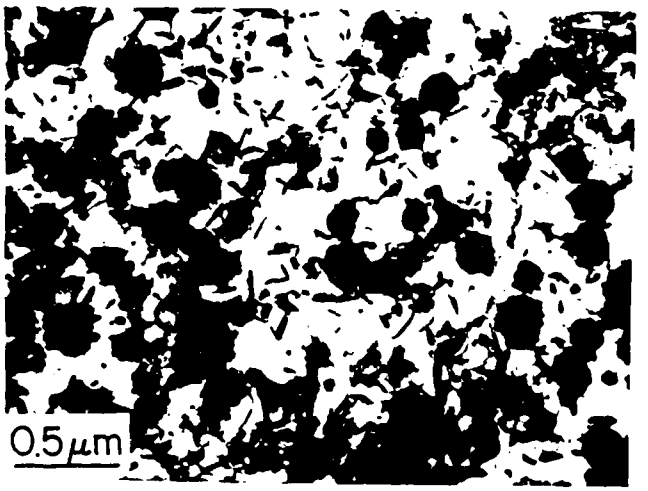

(a)

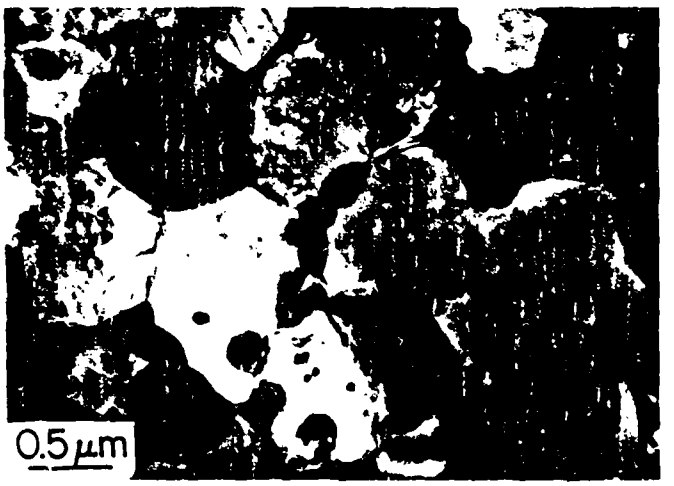

(b)

Fig. 23. Transmission electron micrographs of Al-10Fe-1.5Mo-1V: (a) as-received state and (b) 575°C, 10 hours.

Figures 23a and b are transmission electron micrographs of surface replicas of specimens aged 20 hours at 475° C and 5 hours at 575° C. The particle shapes are much more rounded after aging at the higher temperature, the lower temperature shapes are quite angular.

The mean intercept lengths are shown versus t in Figs. 24 and 25. In these figures $\bar{L}^3$ is plotted versus t following the L-S-W theory. Data for the Alcoa Al-Fe-Ce alloy reported last year are plotted for comparison. It is immediately noticed that the dispersed phase in the Pratt-Whitney Al-Fe-Mo-V alloy coarsens faster than the dispersed phase in the Al-Fe-Ce alloy. This same data is plotted as $\bar{L}$ versus T in Fig. 26. The coarsening rate of the Al-Fe-Mo-V alloy is approximately 30% faster than the Al-Fe-Ce alloy.

Analysis of the data according to the L-S-W theory was attempted with the assumption that the dispersed phase has the formula $(Fe,Mo,V)Al_3$. According to this theory, after a certain amount of coarsening a steady state size distribution is obtained if the size distribution is normalized with respect to the average particle radius. Figures 27 and 28 show that steady state distributions were more or less obtained after 50 hours at 475 or 575° C. Assuming iron diffusion is rate controlling and using the Brailsford and Wynblatt (17) correction for the volume fraction effect on interfacial energy, a value of σ of 0.15 J/m^2 was obtained for coarsening at 575° C, a value consistent with an incoherent interface. If Mo or V diffusion is considered to be rate controlling, then much much larger values of σ are calculated. This result is thought to be due to a failure of the L-S-W theory when applied to quaternary alloys. The L-S-W theory was derived for binary alloys.

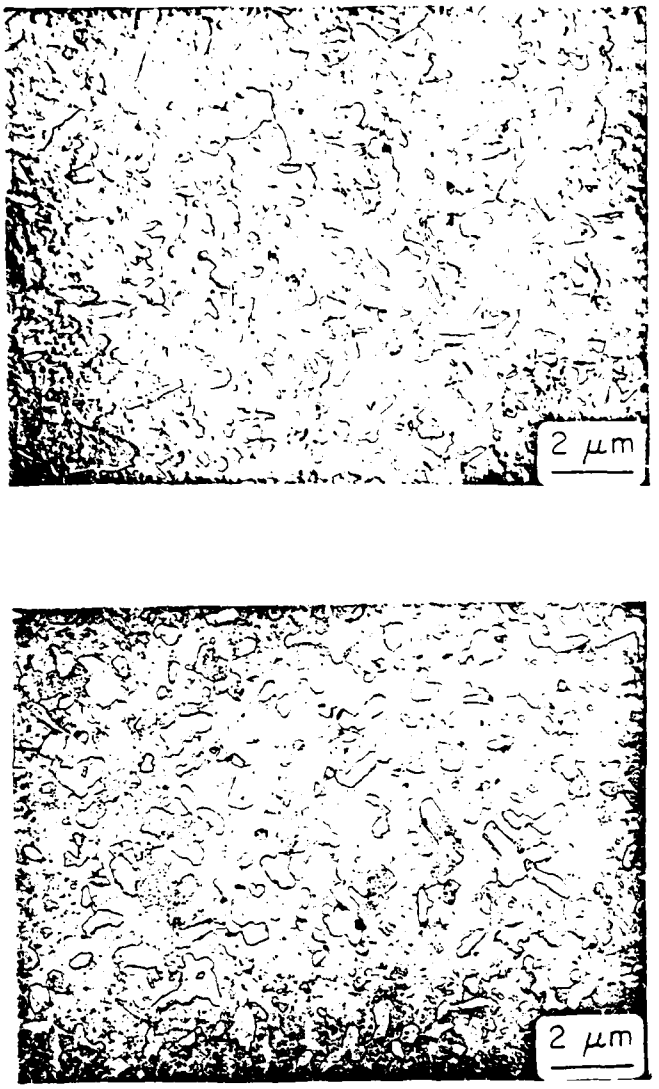

(a)

(b)

Fig. 23. Transmission electron micrographs of surface replicas of Al-Fe-Mo-V alloy coarsened (a) 20 hours at 475° C and (b) 5 hours at 575° C.

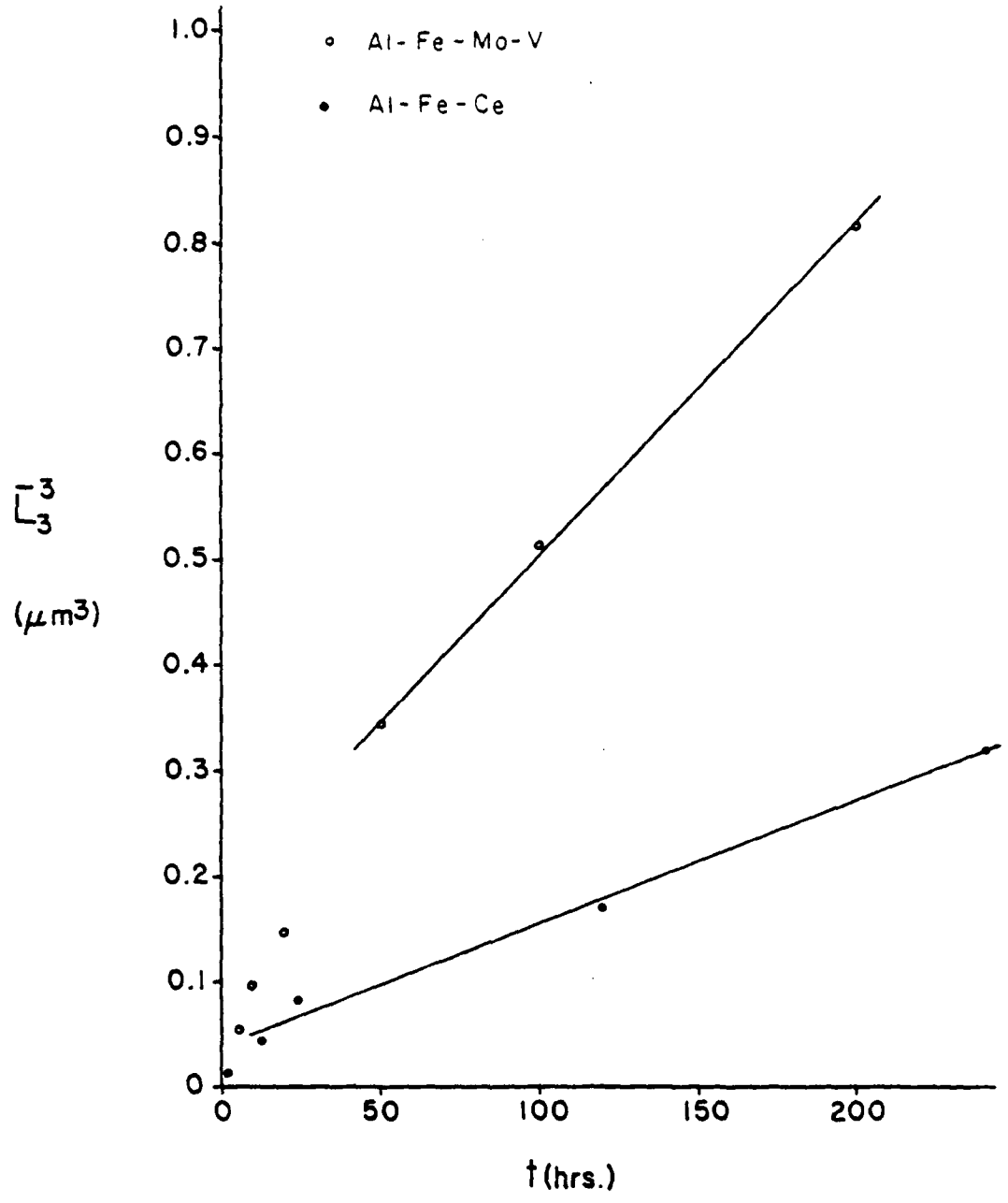

Fig. 24. Plot of $\bar{L}^3$ versus aging time at 575°C.

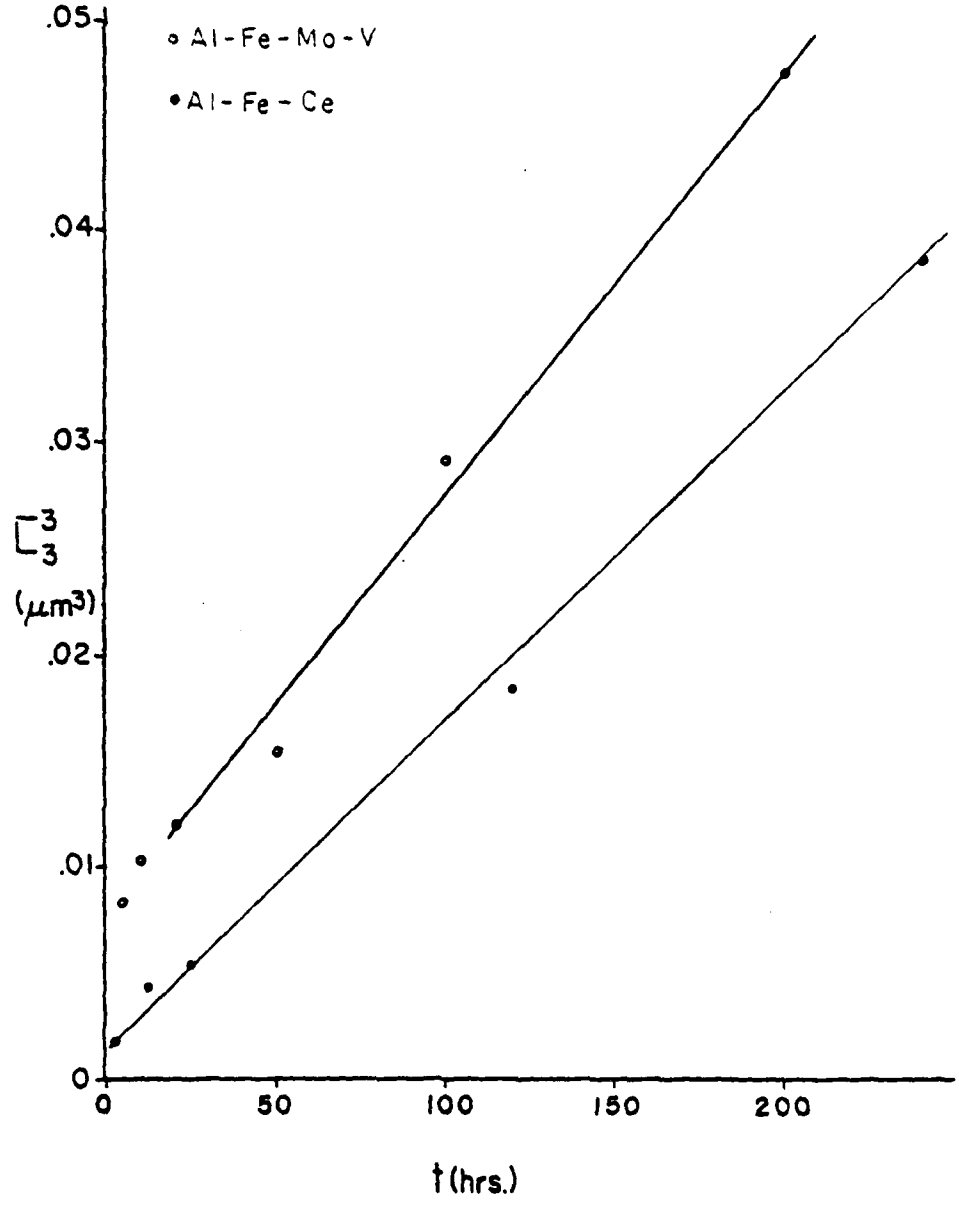

Fig. 25. Plot of $\bar{L}^3$ versus aging time at 475°C.

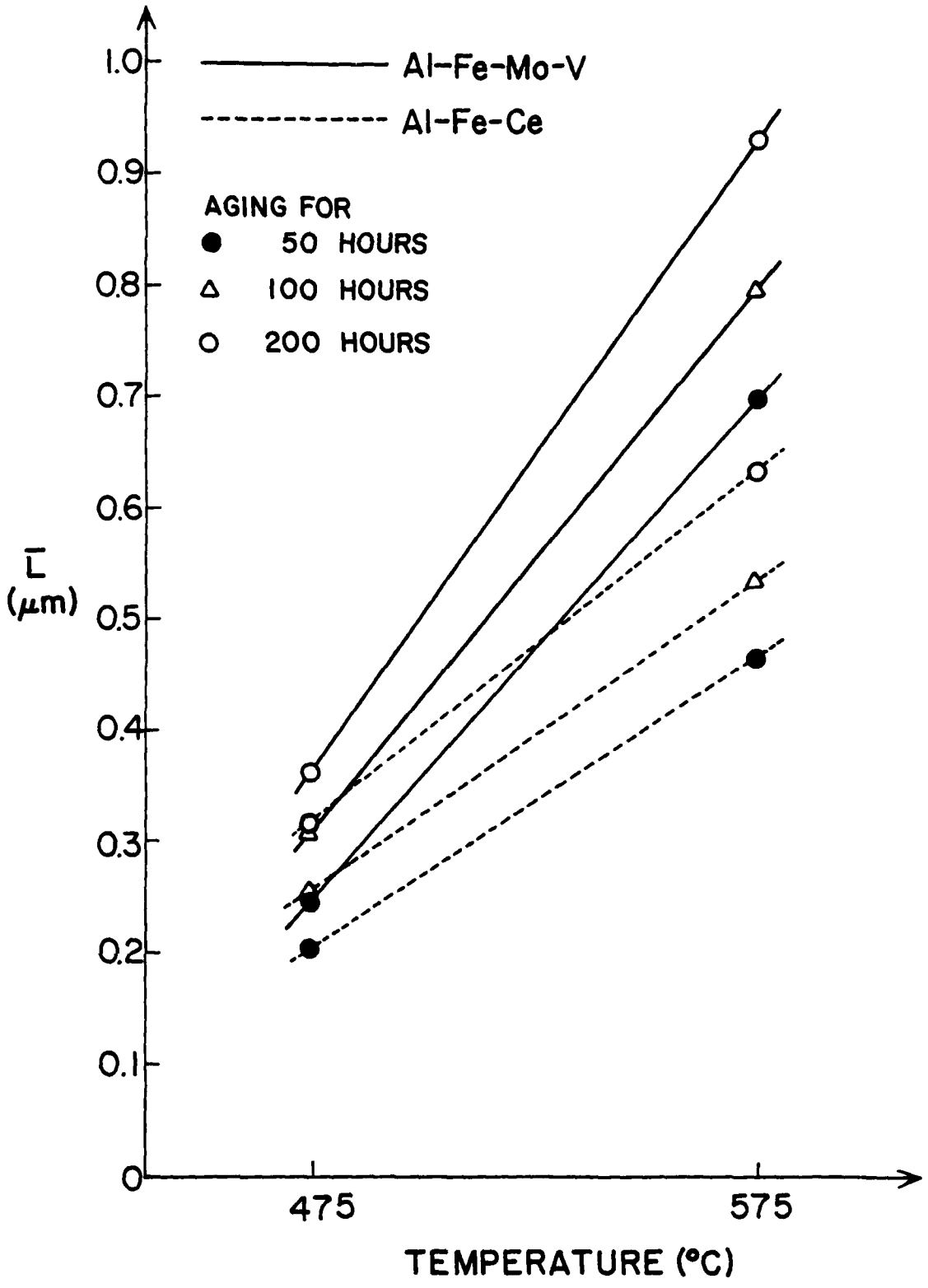

Fig. 26. Average intercept $\bar{L}$ versus temperature for constant aging times of 50, 100 and 200 hours.

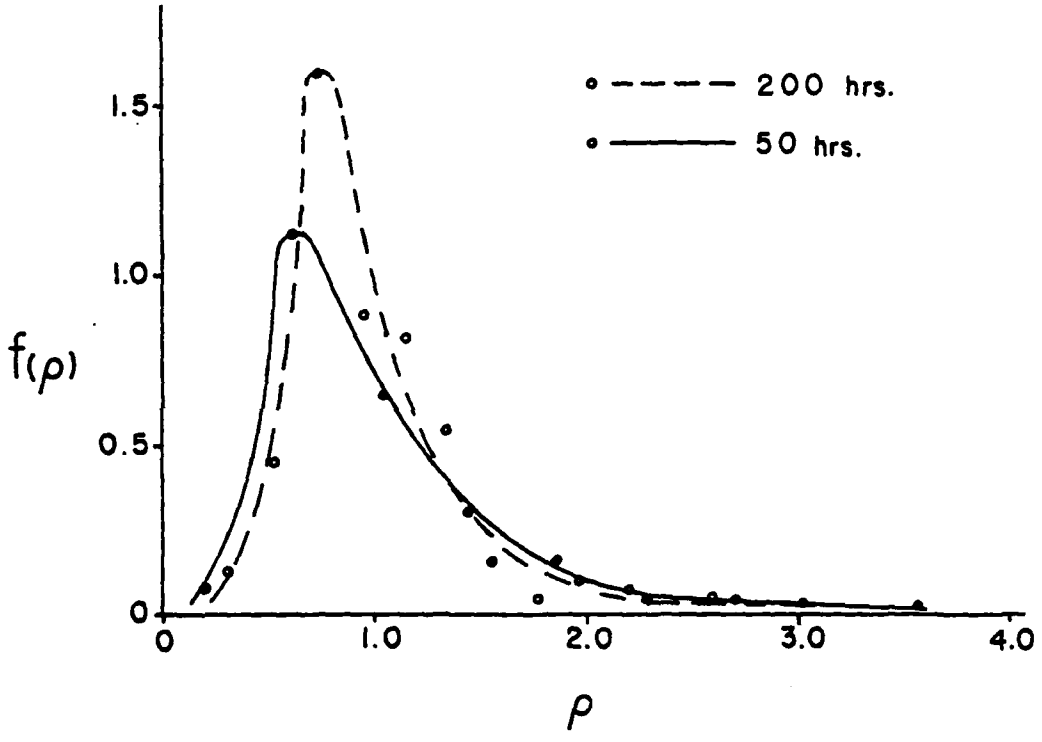

Fig. 27. Particle size distribution versus reduced particle intercept length $L/\bar{L}$ for 50 and 200 hours at 475° C.

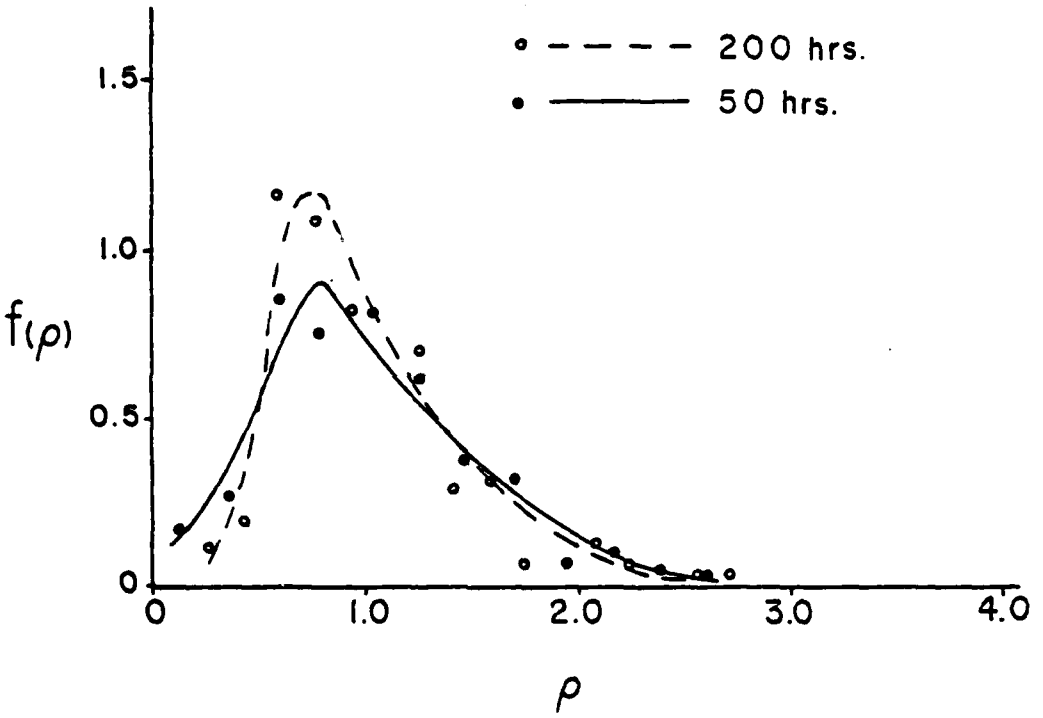

Fig. 28. Particle size distribution versus reduced particle intercept length $L/\bar{L}$ for 50 and 200 hours at 575° C.

References

1. O. S. Zarechnyuk, M. G. Mys'kiv and V. R. Ryabor, Russian Metallurgy, 1969, No. 2, p. 133.
2. E. Bachmetew, Z. Krist. 89, 581 (1934).
3. S. Tsunekawa and M. E. Fine, Scripta Met. 16, 391 (1982).
4. F. J. J. van Loo and G. D. Rieck, Acta Met. 21, 61 (1973).
5. G. Brauer, Z. F. Electrochemie 49, 208 (1943).
6. G. Brauer, Z. anors. Alls. Chem. 242, 1 (1939).
7. A. E. Dwight, J. W. Downey and R. A. Conner, Jr., Acta Cryst. 14, 75 (1961).
8. N. Ryum, J. Inst. Metals 94, 191 (1966).
9. N. Ryum, Acta Met. 17, 269 (1969).
10. O. Izumi and D. Oelschlägel, Scripta Met. 3, 619 (1969).
11. E. Nes and N. Ryum, Scripta Met. 5, 987 (1971).
12. E. Nes, Acta Met. 20, 499 (1972).
13. E. Nes and H. Billdall, Acta Met. 25, 1031 (1977).
14. E. H. Hollingsworth, G. R. Frank, Jr. and R. E. Willett, Trans. Met. Soc. AIME 224, 188 (1962).
15. L. K. Walford, Acta Cryst. 18, 287 (1965).
16. P. J. Black, Acta Cryst. 8, 43 (1955).
17. A. D. Brailsford and P. Wynblatt, Acta Met. 27, 489 (1979).

LIST OF PUBLICATIONS -- AF SUPPORTED

M. E. Fine

1. "Lattice Parameter Variation of $Al_3(Ti,V,Zr,Hf)$ in Al-2 at.% (Ti,V,Zr,Hf) Alloys" (with M. Zedalis), Scripta Met. 17, 1247 (1983).

2. "Fatigue Crack Initiation and Microcrack Propagation in X7091 Type Aluminum P/M Alloys" in High Strength Powder Metallurgy Aluminum Alloys, Proc. of Symposium on Powder Metallurgy of Aluminum Alloys (AIME), M. J. Koczak and G. J. Hildeman, eds., pp. 19-39 (1983). With S. Hirose.

3. "Fatigue Crack Initiation and Microcrack Propagation in X7091 Type Aluminum P/M Alloys" (with S. Hirose), Met. Trans. 14A, 1189 (1983).

4. "The Effect of Aluminum Oxide Particles and Precipitate Type on Near-Threshold Fatigue Crack Propagation Rate in P/M 7XXX Aluminum Alloys" (with M. Zedalis), Scripta Met. 16, 1411 (1982).

5. "The Effect of Dispersoid Type, Purity and Oxide on the Near-Threshold Fatigue Crack Propagation in I/M and P/M 7XXX Al Alloys", Proceedings Volume, TMS-AIME Fall Meeting, St. Louis, 1982 (to appear in Constituent Phases in Al Alloys II, Conf. Proc. Volume). With M. Zedalis, L. Filler and S. I. Kwun).

J. R. Weertman

1. "Deformation-Induced Strain Localization and Residual Stresses Around Hard Particles" (with K. Shiozawa), Proceedings of Workshop on Plasticity of Metals at Finite Strain, June 29-July 1, 1981, E. H. Lee and R. L. Mallett, eds., Stanford University, pp. 648-656 (1982).

2. "Studies of Nucleation Mechanisms and the Role of Residual Stresses in the Grain Boundary Cavitation of a Superalloy" (with K. Shiozawa), Acta Met. 31, 993 (1983).

LECTURES PRESENTED -- AF SUPPORTED

J. R. Weertman

1. "Nucleation of Grain Boundary Voids in a Nickel Base Superalloy", Purdue University, Lafayette, Indiana, 30 November 1982 (invited).

2. "Coarsening of a Dispersed Second Phase in an Aluminum-Iron, Cerium Alloy" (given by L. Angers, with M. E. Fine), AIME Annual Meeting, Atlanta, Georgia, 9 March 1983.

3. "Investigation of a Critical Problem in High Temperature Damage: Nucleation of Grain Boundary Voids", ASTM, Louisville, Kentucky, 9 May 1983 (invited).

4. "Coarsening of a Dispersed Second Phase in an Aluminum-Iron-Cerium Alloy" (given by L. Angers, with J. R. Weertman), Wright-Patterson Air Force Base, Dayton, Ohio, 13 May 1983.

5. "Effect of Room Temperature Prestrain History on the Fatigue Life of Superalloys at High Temperatures", Thermomechanical Fatigue Workshop, NASA-Lewis, Cleveland, Ohio, 21 September 1983 (invited, included work sponsored by NASA).

M. E. Fine

1. "The Effect of Dispersoid Type, Purity and Oxide on the Near-Threshold Fatigue Crack Propagation in I/M and P/M 7XXX Al Alloys" (given by M. Zedalis, with M. E. Fine, L. Filler and S. I. Kwun), TMS-AIME Fall Meeting, St. Louis, Missouri, October 1982.

2. "Design of High Temperature Aluminum Alloys", WESTEC '83 (Western Metal & Tool Exposition & Conference), Los Angeles, CA, March 22, 1983 (invited).

3. "Coarsening of a Dispersed Second Phase in an Aluminum-Iron, Cerium Alloy" (given by L. Angers, with J. R. Weertman), AIME Annual Meeting, Atlanta, Georgia, March 9, 1983.

4. "Research on High Temperature Aluminum Alloys", Northrup Aviation, Los Angeles, CA, January 18, 1983 (invited).

PROFESSIONAL PERSONNEL

1. Professor Morris E. Fine, Principal Investigator

2. Professor Julia R. Weertman, Principal Investigator

3. Dr. Jain-Long Horng, Ph.D. student 10/1/82-7/14/83, Postdoctoral Fellow beginning 7/15/83.

4. Mr. Michael S. Zedalis, Ph.D. student. American Can Fellow 9/1/82-5/30/83, Graduate Research Assistant on grant before and after.

5. Ms. Lynette Angers, Ph.D. student.

6. Mr. Terrence R. Wilkinson, M.S. student 9/15/82-9/30/83.

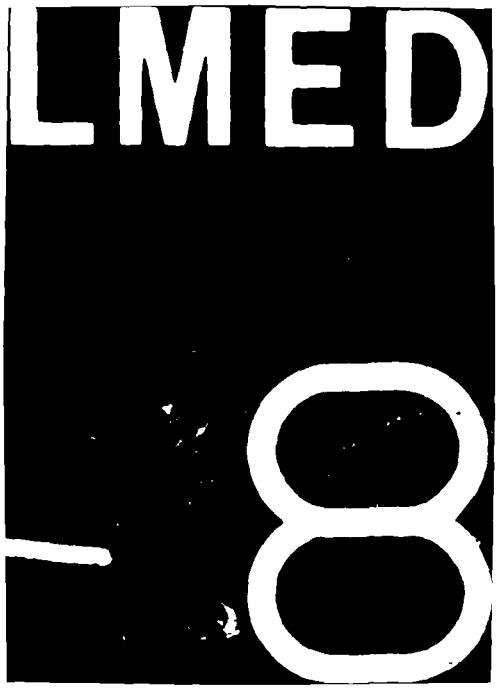
LMED
8